Article

Immunity

Polyamines regulate adaptive antitumor immunity by functional specialization of regulatory T cells

Graphical abstract

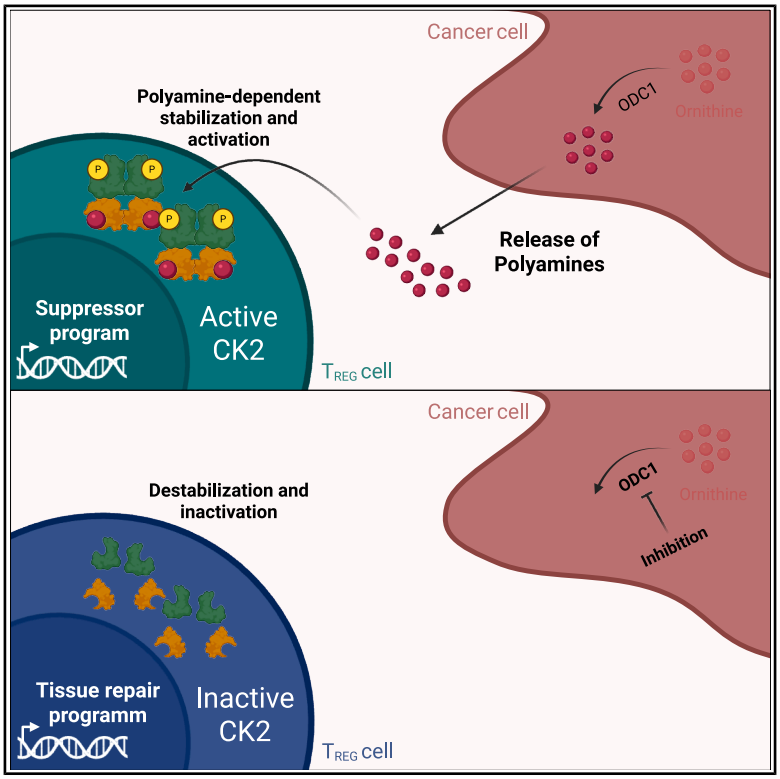

Authors

Georg Bündgen, Alexander Ulges, Jan Pietruschka, ..., Charles Imbusch, Hansjörg Schild, Tobias Bopp

Correspondence

boppt@uni-mainz.de

In brief

Bündgen et al. reveal that polyamines in the tumor environment shift T_{reg} cells toward suppression via CK2 signaling. Blocking this pathway reprograms T_{reg} cells to support tissue repair and antitumor immunity. These findings highlight a potential strategy to rewire immune responses and improve cancer therapies.

Highlights

- Tumor-derived polyamines drive T_{reg} cell immunosuppression in a CK2-dependent manner
- CK2 or tumor polyamine blockade reprograms T_{reg} cells to a tissue repair phenotype
- Blocking tumor-derived polyamines enhances antitumor type 2 immune responses
- Tissue reparative T_{reg} cells support type 2 antitumor immunity and $CD8^+$ T cell fitness

Bündgen et al., 2025, Immunity *58*, 2019–2034
August 12, 2025
https://doi.org/10.1016/j.immuni.2025.07.007

CellPress

Immunity

CellPress
OPEN ACCESS

Article

Polyamines regulate adaptive antitumor immunity by functional specialization of regulatory T cells

Georg Bündgen,[1] Alexander Ulges,[1] Jan Pietruschka,[1] Natalia Truong-Andrievici,[1] Matthias Klein,[1,2] Karolina Romaniuk,[1] Fabian Schmitt,[1] Mathias Hagen,[1] Joachim G. Seebass,[1] Lenart Zezlina,[1] Lara Stein,[1] Hans Christian Probst,[1,2] Ute Distler,[1,2] Stefan Tenzer,[1,2,3] Michael Lohoff,[4] Addi J. Romero-Olmedo,[4] Henrik Mei,[5] Toszka Bohn,[1,2] Michael Delacher,[1,2] Thierry Schmidlin,[1,2] Matthias M. Gaida,[2,6,7,8] Ivan Dikic,[9] Charles Imbusch,[1,2,10,11,12] Hansjörg Schild,[1,2,13,14] and Tobias Bopp[1,2,7,11,12,13,14,15,*]

[1]University Medical Center Mainz, Institute of Immunology, 55131 Mainz, Germany
[2]Research Center for Immunotherapy (FZI), University Medical Center Mainz, 55131 Mainz, Germany
[3]HI-Tron, DKFZ, 69120 Heidelberg, Germany
[4]Philipps University Marburg, Institute for Medical Microbiology and Hospital Hygiene, 35043 Marburg, Germany
[5]Deutsches Rheumaforschungszentrum Berlin, a Leibniz Institute, 10117 Berlin, Germany
[6]University Medical Center Mainz-Institute of Pathology, 55131 Mainz, Germany
[7]University Cancer Center (UCT) Mainz, University Medical Center Mainz, 55131 Mainz, Germany
[8]TRON, 55131 Mainz, Germany
[9]Institute of Biochemistry II, Medical Faculty, Goethe University, 60590 Frankfurt am Main, Germany
[10]Division of Applied Bioinformatics, German Cancer Research Center (DKFZ), 69120 Heidelberg, Germany
[11]Institute for Quantitative and Computational Biosciences (IQCB), 55128 Mainz, Germany
[12]German Cancer Consortium (DKTK), 69120 Heidelberg, Germany
[13]Centre for Healthy Ageing, Johannes Gutenberg University Mainz, 55128 Mainz, Germany
[14]These authors contributed equally
[15]Lead contact
*Correspondence: boppt@uni-mainz.de
https://doi.org/10.1016/j.immuni.2025.07.007

SUMMARY

In cancer, metabolic changes and uncontrolled tumor growth alter nutrient availability, impacting antitumor immune responses. Regulatory T (T_{reg}) cells are a subset of T cells with immunosuppressive properties that can also influence tissue homeostasis and repair. However, it is not known how these functions are molecularly controlled and whether they are influenced by tumor metabolism. Here, we report that excessive release of polyamines in the tumor microenvironment directs the functional polarization of T_{reg} cells toward immunosuppression in a protein kinase CK2 (CK2)-dependent manner. Polyamine deprivation as well as genetic or pharmacological inhibition of CK2 activity in T_{reg} cells induced tissue reparative properties in T_{reg} cells that orchestrated efficient antitumor type 2 immune responses and coordinated tissue repair mechanisms to support tumor eradication. These findings suggest that targeted modulation of T_{reg} cell functions could be leveraged as a potential avenue for cancer therapy.

INTRODUCTION

Tissue repair and cancer share cellular and molecular processes that are tightly regulated in physiological tissue conditions but deregulated and thought to be exploited by tumors for uncontrolled growth. To this end, tumors have developed manifold evasion strategies to avoid an effective antitumor immune response. For example, deregulated metabolic activity of tumor cells can result in deprivation of key nutrients required for efficient antitumor immunity and the accumulation of metabolites, contributing to tumor immune evasion.[1] Furthermore, the competition among tumor cells also leads to cell death and the subsequent uncontrolled release of intracellular substances, including metabolites.[2–4]

The polyamines putrescine, spermidine, and spermine were detected in elevated concentrations in the urine of patients with cancer more than 40 years ago[5] and have long been considered as diagnostic markers for cancer. Inhibition of polyamine production combined with inhibition of polyamine transport using a novel inhibitor, AMXT 1501 Dicaprate, is being tested in a phase 1 clinical trial to abrogate polyamine-dependent anabolism in solid cancer (source: ClinicalTrials.gov ID: NCT05500508). However, little is known about the molecular mechanisms evoked by polyamines in tumor-infiltrating leukocytes (TILs).

Polyamines are centrally involved in fundamental cell biology processes, including maintenance of protein and nucleic acid synthesis, stabilization of chromatin structure,

apoptosis, and cell differentiation.[6,7] In addition to their involvement in anabolic processes, polyamines also stabilize and activate kinases to regulate intracellular signal transduction pathways.

Polyamines have been identified as potent activators of protein kinase CK2.[8] *In vitro* studies have shown that this activation is strictly dependent on the presence of the β subunit (CK2β), encoded by *Csnk2b*.[9] Structural analyses of human CK2β revealed an acidic groove that likely serves as a docking site for basic polypeptide regions.[10] Binding of polyamines to this groove has been shown to enhance CK2 enzymatic activity,[11] and subsequent studies have demonstrated that polyamines can increase holoenzyme activity several-fold.[12–15]

Polyamines prevent autoimmunity, and inhibition of their synthesis drives regulatory T (T_{reg}) cell differentiation by enhancing expression of the transcription factor FOXP3.[16] T_{reg} cell-specific deficiency in CK2β enhances T helper (T_H) 2 cell immune responses.[17] T_{reg} cells are capable of suppressing almost all types of immune responses by regulating the activities of most innate and adaptive immune cell types.[18] In the cancer context, T_{reg} cells are overrepresented in many different tumors and are generally associated with a poor prognosis due to their immunosuppressive properties. T_{reg} cells are also critical for tissue homeostasis and can modulate host metabolism and tissue repair mechanisms. Thus, T_{reg} cells exert important functions beyond preventing allergy, autoimmunity, or tumor immune evasion.[19]

While publications show that human T_{reg} cells can produce inflammatory cytokines in the tumor microenvironment (TME),[20,21] they are still considered to suppress efficient antitumor immunity.[22–24]

How their diverse immunoregulatory functions are controlled in the context of tumors and what effects each of these functions has on tumor growth is not fully understood. In this study, we sought to identify the role of tumor-derived polyamines in functional polarization of T_{reg} cells. In particular, we wanted to understand the possibility to separately modulate suppressive and tissue reparative properties attributed to T_{reg} cells. Here, we demonstrated that polyamines in the TME repressed the tissue reparative properties of T_{reg} cells and enhanced their immunosuppressive function in a CK2β-dependent manner. In this way, we separately modulated T_{reg} cell functions related to tissue homeostasis, control of autoimmunity, and suppression of efficient antitumor immunity. Pharmaceutical inhibition or genetic ablation of CK2β in T_{reg} cells enabled their immunoregulatory tissue repair function and unleashed a coordinated antitumor type 2 immune response. These results reveal how T_{reg} cells can be leveraged beyond their immunosuppressive functions to clinically exploit their reparative functions for effective antitumor immune response.

RESULTS

Tumor-produced polyamines regulate the adaptive antitumor immune response

To assess tumor-derived metabolites, wild-type (WT) mice were subcutaneously (s.c.) injected with B16.F10 melanoma (B16.F10) cells or MC38 colon adenocarcinoma (MC38) cells. Tumors were excised at ~200 mm^3 and flushed with PBS to collect interstitial fluid for quantitative mass spectrometry (see STAR Methods). This revealed an abundance of several metabolites in the TME (Figure S1A), including strongly elevated levels of putrescine, spermine, and spermidine compared with healthy skin (Figures 1A and S1B). In line with this, increased serum polyamine concentrations in tumor-bearing mice mirrored findings in human patients, indicating enhanced tumor-derived polyamine release (Figure 1B). To further assess relevance to human tumors, we analyzed data from the Cancer Genome Atlas (TCGA), revealing high expression of polyamine anabolic enzymes in tumor tissue (Figures S1C and S1D). Furthermore, high expression of enzymes promoting polyamine synthesis (ODC1, SRM, SMS, AZIN1, and AMD1) correlated with poor survival, whereas elevated expression of catabolic enzymes (SAT1, PAOX, SMOX, and OAZ1–3) predicted improved outcomes (Figures S1E and S1F). Given our interest in polyamine-driven suppression of adaptive immunity, we selected the low-immunogenic, aggressively growing B16.F10 melanoma model.

In light of the role of polyamines as diagnostic biomarkers in cancer, we investigated how elevated interstitial polyamine levels in the TME affect tumor progression. While complete germline deletion of ODC1, the rate-limiting enzyme in polyamine biosynthesis, causes B16.F10 cell death *in vitro*, we instead inhibited ODC1 using difluoromethylornithine (DFMO) or small interfering RNA (siRNA) to study tumor-derived polyamines in immune responses. B16.F10 cells were treated with DFMO or transfected with *Odc1*-specific siRNA prior to s.c. inoculation into C57BL/6J WT mice. Inhibition of ODC1 using DFMO reduced intracellular levels of spermidine and spermine and caused accumulation of arginine, the precursor of L-ornithine, which is the substrate of ODC1 (Figure 1C). This metabolic blockade led to reduced tumor growth *in vivo* (Figure 1D), indicating a possible direct effect on tumor cell proliferation, antitumor immunity, or both. Likewise, *Odc1*-silencing with siRNA decreased polyamine production and limited tumor progression (Figures S1G–S1I). Analysis of tumor-infiltrating $CD4^+$ T cells revealed a T_H2-skewed response upon ODC1 inhibition, with increased $GATA3^+$ and interleukin (IL)-4^+ but unchanged interferon (IFN)-γ^+ cells (Figures 1E–1G and S1J), suggesting polyamines suppress type 2 immunity. To assess how polyamine deprivation in the TME affects T_{reg} cells modulating type 2 immunity, we analyzed immunoglobulin-like transcript (ILT)3-expressing T_{reg} cells among TILs in DFMO-treated or ODC1-silenced tumors and respective controls. $ILT3^+$ T_{reg} cells, a subset unable to suppress type 2 immunity,[17,25] were increased in the TME following polyamine synthesis inhibition (Figures 1H and S1K). The development and T_H2-promoting function of $ILT3^+$ T_{reg} cells depend on CK2β, which regulates holoenzyme assembly and kinase activity.[17] *In vitro*, polyamines bind to threonine 72 of CK2β, near a glutamic acid tripeptide (E60/61/63) adjacent to the catalytic pocket. This binding induces a conformational shift that enhances substrate access and CK2 phosphorylation activity.[11,12,26] To substantiate our findings, we performed molecular docking using SwissDock and visualized predicted polyamine binding to CK2β with chimera,[27] identifying the acidic groove as the main binding site (Figure S1L), confirming findings by Leroy et al.[11] To assess the role of polyamines in regulating CK2 activity in T_{reg} cells, we cultured WT T_{reg} cells with either the

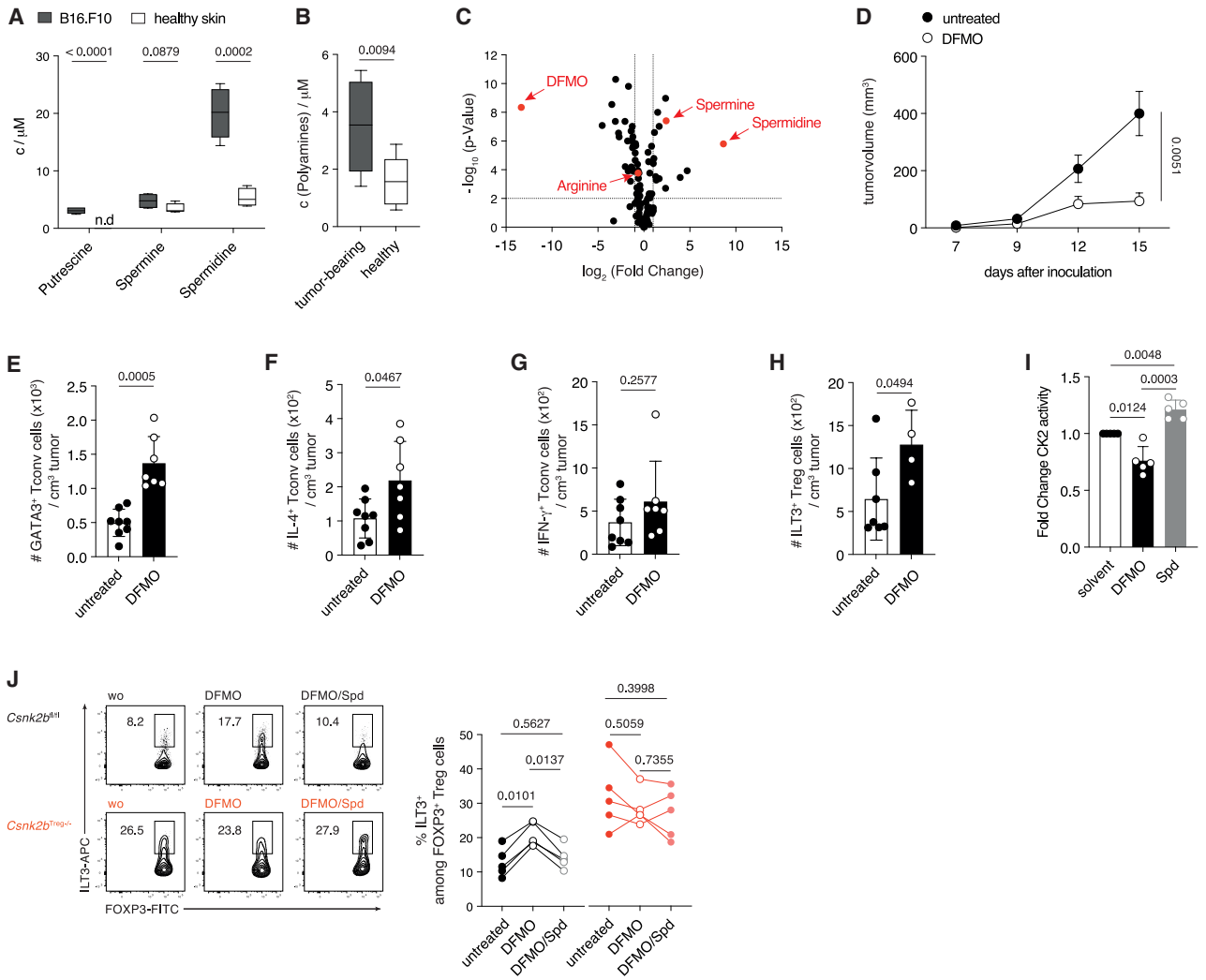

Figure 1. Tumor-derived polyamines suppress anti-tumoral type 2 immunity

(A) Interstitial polyamine levels in flushed B16.F10 tumors (n = 6) and healthy skin (n = 4) (n.d., not detectable).

(B) Serum polyamine levels in tumor-bearing and healthy mice (n = 8/group).

(C) Volcano plot of metabolomic profiles from untreated vs. DFMO-treated B16.F10 cells (n = 7/group; significance: fold change (FC) > 2, p < 0.05). Metabolites of interest and DFMO are highlighted in red.

(D) Tumor growth kinetics of WT mice inoculated with untreated or DFMO-pretreated B16.F10 cells (n = 8/group).

(E–H) Total numbers of live CD45$^+$TCRβ$^+$CD4$^+$FOXP3$^-$GATA3$^+$ (E), IL-4$^+$ (F) and IFN-γ$^+$ (G) T_{conv} cells (untreated n = 8, DFMO-treated n = 7) as well as total numbers of live CD45$^+$TCRβ$^+$CD4$^+$FOXP3$^+$ILT3$^+$ T_{reg} cells (H) (untreated n = 7, DFMO-treated n = 4) per cm^3 tumor.

(I) CK2 activity fold change in WT T_{reg} cells treated with 1 mM DFMO or 2.5 µM spermidine (Spd) (n = 5/group).

(J) Representative flow cytometry plots and quantification of ILT3$^+$ T_{reg} cells in cultures of WT (*Csnk2b*$^{fl/fl}$) or CK2β-deficient (*Csnk2b*$^{Treg-/-}$) T_{reg} cells cultured with 1 mM DFMO alone or in combination with 2.5 µM Spd for (n = 5/group). Lines connect untreated and DFMO- and DFMO/Spd-treated samples from the same biological replicate. Total cell numbers were quantified on day 15 post s.c. B16.F10 cell injection. Tumor growth (D) is shown as mean ± SEM. Data in box (A) and (B) and box dot plots (E–I) are shown as mean ± SD with individual biological replicates (E–I) plotted. Statistical significance was determined using two-tailed unpaired t tests with Welch's correction. p values are indicated in the figure.

See also Figure S1.

ODC1 inhibitor DFMO or exogenous spermidine. DFMO reduced, whereas spermidine enhanced CK2 holoenzyme activity (Figure 1I), indicating a specific regulatory mechanism. Furthermore, DFMO treatment increased ILT3 expression on T_{reg} cells, which was reversed by spermidine. This regulation was absent in CK2β-deficient T_{reg} cells (Figure 1J), confirming that polyamine-mediated modulation of ILT3 expression depends on CK2β activity.

T_{reg} cell-specific CK2β deficiency promotes efficient antitumor immunity

To define the functional relevance of CK2β in polyamine-regulated T_{reg} cell activity, we used *Csnk2b*$^{Treg-/-}$ mice (*Csnk2b*$^{fl/fl}$ *Foxp3*-IRES-Cre), in which CK2β is selectively ablated in FOXP3$^+$ T_{reg} cells. These mice were born at Mendelian ratios, appeared phenotypically normal, and showed unaltered thymic T_{reg} cell development, homeostasis, and polyamine synthesis

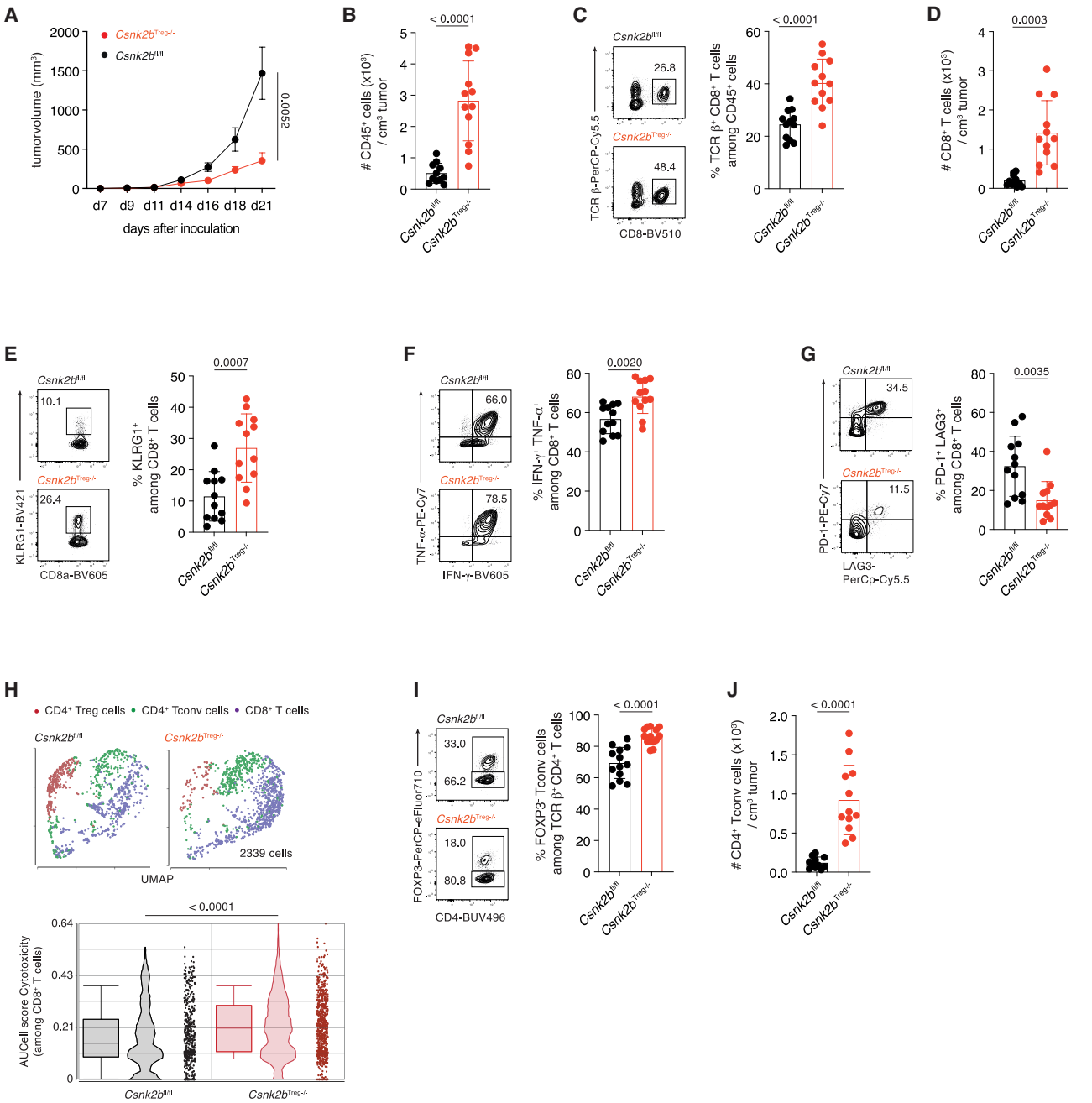

Figure 2. T_{reg} cell-specific CK2β deficiency promotes efficient antitumor immunity

(A) Tumor growth kinetics of B16.F10 tumors in *Csnk2b*$^{fl/fl}$ mice (n = 15) and *Csnk2b*$^{Treg-/-}$ mice (n = 17).

(B) Total numbers of live CD45$^+$ cells in B16.F10 tumors (per cm^3 tumor) of *Csnk2b*$^{fl/fl}$ (n = 11) and *Csnk2b*$^{Treg-/-}$ (n = 12) mice.

(C) Representative flow cytometry plots and quantification of CD8$^+$ T cells (TCRβ$^+$CD8$^+$ among CD45$^+$ live cells) in tumors of *Csnk2b*$^{fl/fl}$ and *Csnk2b*$^{Treg-/-}$ mice (n = 12/group).

(D) Total numbers of live CD45$^+$TCRβ$^+$CD8$^+$ T cells in tumors (per cm^3 tumor) of *Csnk2b*$^{fl/fl}$ (n = 11) and *Csnk2b*$^{Treg-/-}$ (n = 12) mice.

(E–G) Representative flow cytometry plots and quantification of KLRG1$^+$CD8$^+$ T cells (E), IFN-γ$^+$TNF-α$^+$CD8$^+$ T cells (F), and PD-1$^+$LAG-3$^+$CD8$^+$ T cells (PD-1$^+$LAG-3$^+$ among CD45$^+$TCRβ$^+$CD8$^+$ T cells) (G) in tumors of *Csnk2b*$^{fl/fl}$ and *Csnk2b*$^{Treg-/-}$ mice (n = 12/group).

(H) scRNA-seq analysis of tumor-infiltrating T cells of *Csnk2b*$^{fl/fl}$ and *Csnk2b*$^{Treg-/-}$ mice (n = 3/group). Uniform manifold approximation and projection (UMAP) visualization (upper) and AUCell-based cytotoxic gene signature enrichment in CD8$^+$ T cells (lower).

(I) Representative flow cytometry plots and quantification (right) of CD4$^+$FOXP3$^-$ T_{conv} cells (FOXP3$^-$ among TCRβ$^+$CD4$^+$ T cells) in tumors of *Csnk2b*$^{fl/fl}$ and *Csnk2b*$^{Treg-/-}$ mice (n = 13/group).

(legend continued on next page)

(Figures S2A–S2C). CK2β-deficiency markedly reduced CK2 holoenzyme activity in T_{reg} cells (Figure S2D). To assess whether this affected cellular fitness, we generated mixed bone marrow chimeras using equal parts of CD90.2$^+$ *Csnk2b*$^{Treg-/-}$ and CD90.1$^+$ WT bone marrow. 8 weeks post-engraftment, both T_{reg} cell populations were equally represented in peripheral lymph nodes (Figure S2E), indicating preserved competitive fitness despite CK2β loss.

After ruling out any influence of CK2β deficiency on the fitness of T_{reg} cells, we s.c. inoculated mice with B16.F10 cells and observed greatly reduced tumor growth in *Csnk2b*$^{Treg-/-}$ mice compared with littermate controls (*Csnk2b*$^{fl/fl}$) (Figure 2A). Reduced tumor growth was accompanied by enhanced infiltration of CD45$^+$ immune cells in the TME (Figure 2B), indicating a stronger antitumor response. To assess the antitumor immune response at the single-cell level, we quantified the percentage and number of cytotoxic CD8$^+$ T cells (CTLs) among TILs. This analysis demonstrated an enhanced percentage and number of CTLs (Figures 2C and 2D), indicating enhanced tumor cell killing. Among tumor-infiltrating CTLs in *Csnk2b*$^{Treg-/-}$ mice, we found increased polyfunctional CTLs, as indicated by an increased KLRG1 expression (Figure 2E), increased co-expression of IFN-γ and tumor necrosis factor alpha (TNF-α) (Figure 2F), and a reduced percentage of PD-1$^+$LAG-3$^+$CD8$^+$ T cells (Figure 2G). Programmed cell death protein 1 (PD-1) expression on CK2β-deficient T_{reg} cells was also downregulated (Figure S2F). Single-cell RNA sequencing (scRNA-seq) of αβ T cells from the TME revealed higher expression of cytotoxicity-associated genes in CTLs from *Csnk2b*$^{Treg-/-}$ mice compared with controls (Figure 2H). In line with these findings, we observed increased percentages and numbers of CD4$^+$FOXP3$^-$ effector T cells (T_{conv} cells) (Figures 2I and 2J).

In order to analyze whether this strong antitumor immune response resulted from impaired suppressive properties of CK2β-deficient T_{reg} cells, we analyzed expression of molecules associated with T_{reg} cell suppressive function. This analysis demonstrated unaltered expression of CTLA-4, Granzyme B (GrzB), CD39, and CD73 (Figure S2G) and slightly enhanced expression of IL-10 and transforming growth factor β (TGF-β) (Figure S2H), suggesting unaltered suppressive properties. To functionally test the suppressive properties of CK2β-deficient T_{reg} cells, we isolated T_{reg} cells from *Csnk2b*$^{Treg-/-}$ and *Csnk2b*$^{fl/fl}$ mice and cocultured these cells with naive CTLs and CD11c$^+$ dendritic cells (DCs) isolated from C57BL/6J WT mice. These analyses demonstrated equal suppressive capacity to inhibit CTL proliferation (Figure S2I) and IFN-γ production (Figure S2J) by CK2β-deficient and CK2β-competent T_{reg} cells *in vitro*. Likewise, CK2β-deficient T_{reg} cells showed equal suppressive capacity for inhibiting IFN-γ production by T_H1 cells when compared with CK2β-competent T_{reg} cells (Figure S2K). To test the suppressive capacity of CK2β-deficient T_{reg} cells *in vivo*, we employed a model of T cell-driven colitis. We observed equal suppressive capacity of WT and CK2β-deficient T_{reg} cells for inhibiting colitis induced by the adoptive transfer of naive CD62L^{high}CD44$^-$CD4$^+$ T cells into *Rag1*-deficient host mice, as indicated by their capacity to prevent inflammation-dependent weight loss (Figure S2L).

Together, these findings clearly demonstrate that the polyamine-dependent activation of CK2 in T_{reg} cells impairs efficient adaptive antitumor immunity.

ILT3$^+$ T_{reg} cells orchestrate an efficient type 2 antitumor immune response

To evaluate the role of CK2β in T_{reg} cells in polyamine-dependent suppression of antitumor type 2 immune responses, we analyzed the cellular composition of the CD4$^+$ T cell compartment in the TME of *Csnk2b*$^{Treg-/-}$ and *Csnk2b*$^{fl/fl}$ mice. Therefore, we inoculated *Csnk2b*$^{Treg-/-}$ and *Csnk2b*$^{fl/fl}$ mice with B16.F10 cells and surgically removed tumors 21 days post-inoculation. T_{conv} cells were then isolated for whole transcriptome analysis by RNA sequencing (RNA-seq). Analysis of the differentially expressed genes (DEGs) revealed strong expression of genes associated with a T_H2 phenotype in tumor-infiltrating T_{conv} cells (Figure 3A; Table S1). To substantiate these findings on the cellular level, we analyzed the presence of T_H2 cells in the TME of *Csnk2b*$^{Treg-/-}$ and *Csnk2b*$^{fl/fl}$ mice by multicolor flow cytometry. This analysis showed strongly increased percentages of GATA3-, IL-4-, IL-5-, and IL-13-expressing T_H2 cells, supporting the results obtained by RNA-seq of tumor-infiltrating T_{conv} cells (Figure 3B).

To evaluate the relevance of transcriptome-wide differences in T_{conv} cells from the TME of tumor-bearing *Csnk2b*$^{Treg-/-}$ mice for antitumor immunity, we performed bioinformatic analysis of DEGs with higher expression in tumor-infiltrating T_{conv} cells of *Csnk2b*$^{Treg-/-}$ mice. To assess clinical significance, we correlated these genes with melanoma patient outcomes using TCGA data. A gene signature (Table S2) was generated and subjected to survival analysis based on its expression in TCGA skin cutaneous melanoma (SKCM) datasets via Gene Expression Profiling Interactive Analysis (GEPIA) 2. These analyses demonstrated that the observed transcriptomic changes in T_{conv} cells from the TME of tumor-bearing *Csnk2b*$^{Treg-/-}$ mice strongly correlated with enhanced percent survival in melanoma patients (Figure 3C). These findings suggest that CK2β deficiency in T_{reg} cells and concomitantly enhanced T_H2-driven antitumor immune responses may have cross-species relevance.

To understand the etiology of this adaptive type 2 immunity, we conducted flow cytometry-based analyses of antigen-presenting cells in the TME. These analyses demonstrated an enhanced percentage of a subpopulation of DCs in the TME expressing interferon regulatory factor 4 (IRF4) and programmed cell death 1 ligand 2 (PD-L2) (Figure 3D) to support T_H2 cell differentiation. To understand the effects of enhanced development of type 2 immune responses in the TME on the myeloid antitumor immune response, we analyzed granulocytes by multicolor flow cytometry. We observed strong infiltration of

(J) Total numbers of live CD45$^+$TCRβ$^+$CD4$^+$FOXP3$^-$ T_{conv} cells in tumors (per cm^3 tumor) of *Csnk2b*$^{fl/fl}$ (n = 11) and *Csnk2b*$^{Treg-/-}$ (n = 12) mice. Quantification of total cell numbers, flow cytometry, and scRNA-seq of tumor-infiltrating immune cells was performed on day 21 post s.c. B16.F10 cell injection. Tumor growth (A) is shown as mean ± SEM. Data in box dot plots (B–G, I, and J) are shown as mean ± SD with individual biological replicates plotted. Statistical significance was assessed using two-tailed unpaired t tests with Welch's correction. p values are indicated in the figure.
See also Figure S2.

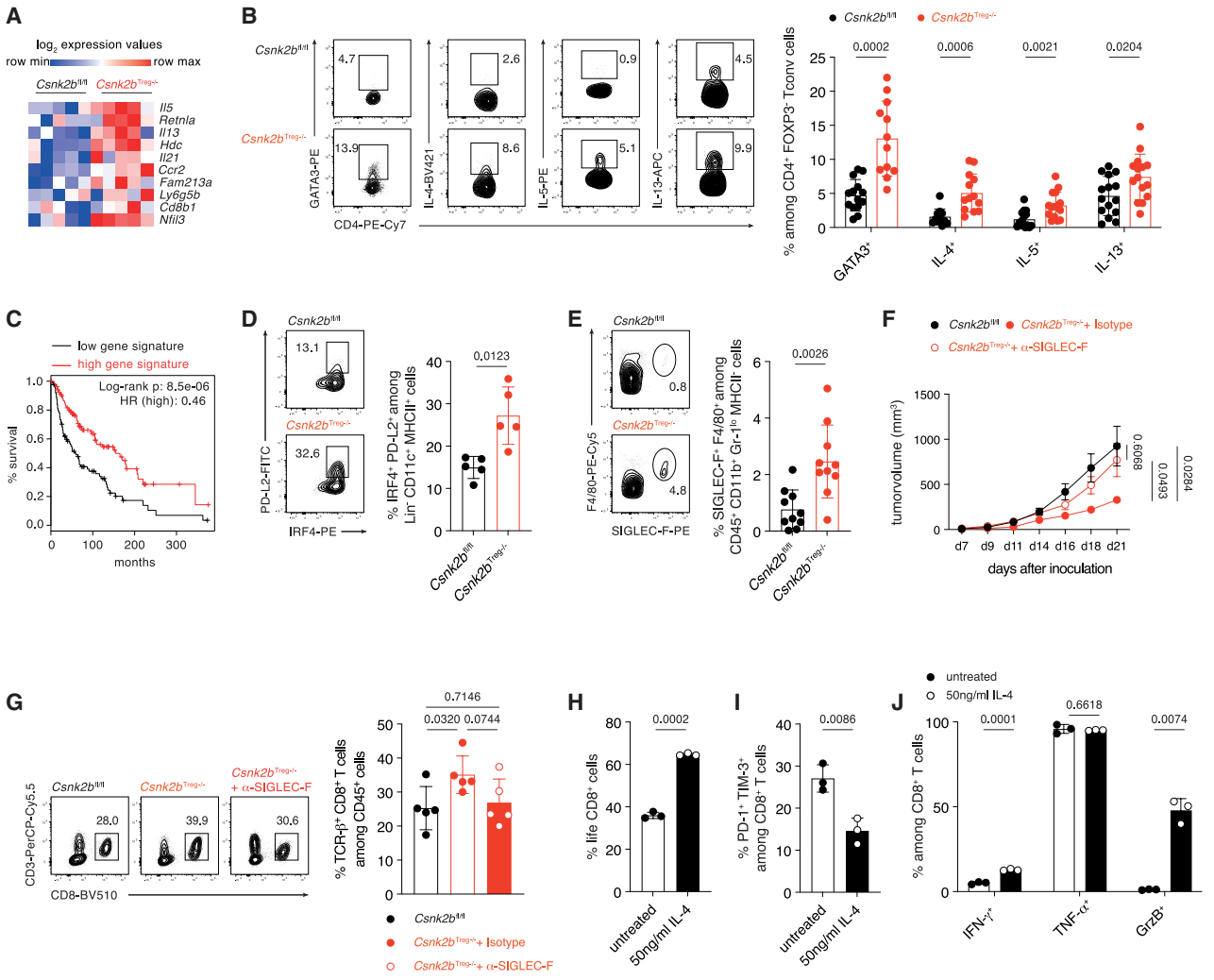

Figure 3. Ablation of *Csnk2b* in T_{reg} cells results in anti-tumoral type 2 immunity

(A) Expression of indicated T_H2-associated genes in tumor-infiltrating CD45$^+$TCRβ$^+$CD4$^+$ T_{conv} cells from *Csnk2b*$^{fl/fl}$ mice and *Csnk2b*$^{Treg-/-}$ mice (n = 5/group; Table S1).

(B) Representative flow cytometry plots and quantification of GATA3$^+$, IL-4$^+$, IL-5$^+$, and IL-13$^+$CD4$^+$ T_{conv} cells (percent among TCRβ$^+$CD4$^+$FOXP3$^-$ T cells) in tumors of *Csnk2b*$^{fl/fl}$ (GATA3: n = 14; IL-4: n = 12; IL-5: n = 15; IL-13: n = 15) and *Csnk2b*$^{Treg-/-}$ mice (GATA3: n = 12; IL-4: n = 13; IL-5: n = 15; IL-13: n = 15).

(C) Kaplan-Meier curve for SKCM patients stratified by high vs. low T_H2 gene signature (33 genes; n = 138/group; log rank p value for hazard ratio [HR] = 1.4e−05; Table S2).

(D and E) Representative flow cytometry plots and quantification of IRF4$^+$PD-L2$^+$ DCs (D) (n = 5/group) and SIGLEC-F$^+$ F4/80$^+$ eosinophils (E) (n = 10/group) in tumors of *Csnk2b*$^{fl/fl}$ and *Csnk2b*$^{Treg-/-}$ mice.

(F) Tumor growth kinetics of B16.F10 tumors in untreated *Csnk2b*$^{fl/fl}$ mice (*Csnk2b*$^{fl/fl}$; n = 9) and *Csnk2b*$^{Treg-/-}$ mice treated with α-SIGLEC-F (*Csnk2b*$^{Treg-/-}$ + α-SIGLEC-F; n = 8) or respective control (*Csnk2b*$^{Treg-/-}$ + isotype; n = 7).

(G) Representative flow cytometry plots and quantification of CD8$^+$ T cells in tumors of *Csnk2b*$^{fl/fl}$, *Csnk2b*$^{Treg-/-}$, and α-SIGLEC-F-treated *Csnk2b*$^{Treg-/-}$ mice (n = 5/group).

(H–J) *In vitro* stimulation of CD8$^+$ T cells with αCD3/28 ± IL-4 for 6 days (n = 3/group). Percentage quantification of viable CD8$^+$ T cells (H), CD8$^+$ T cells co-expressing PD-1 and TIM-3 (I), and CD8$^+$ T cells expressing IFN-γ, TNF-α, or GrzB (J). Flow cytometry was performed on day 21 post s.c. B16.F10 cell injection. Tumor growth (F) is shown as mean ± SEM. Data in box dot plots (B, D, E, and G–J) are shown as mean ± SD with individual biological replicates plotted. Statistical significance was assessed using two-tailed unpaired t tests with Welch's correction. p values are indicated in the figures.

See also Figure S3.

eosinophils into the TME, which likely occurred in response to T_H2 cell-derived IL-5 and IL-13 (Figure 3E).

To understand the role of the observed enhanced type 2 immunity and eosinophil recruitment, we depleted eosinophils *in vivo* by administering α-sialic acid binding Ig-like lectin (SIGLEC)-F antibody, as detailed by Carretero et al.[28] Flow cytometry analyses and t-distributed stochastic neighbor embedding (tSNE)-based visualization demonstrated an almost complete absence of eosinophils upon α-SIGLEC-F treatment (Figures S3A and S3B). Furthermore, depletion of eosinophils

in *Csnk2b*$^{Treg-/-}$ mice resulted in impaired antitumor immunity (Figure 3F) and a reduced percentage of CTLs in the TME (Figure 3G), further dampening efficient antitumor immunity.

Antitumor type 2 immunity prevents CTL exhaustion

Current cancer immunotherapy, including immune checkpoint blockade, focuses on enhancing type 1 immunity to eradicate cancer cells. While these approaches have achieved clinical success, it remains poorly understood how to prevent CTL exhaustion, where cancer-reactive T cells lose functionality and fail to control tumor growth.[29] To understand how a T_{reg} cell-regulated type 2 immune response can control polyfunctionality of CTLs in tumors of *Csnk2b*$^{Treg-/-}$ mice, we established a chronic *in vitro* exhaustion model according to Satpathy and colleagues.[30] Upon stimulation, cells were harvested, and exhaustion was measured by analyzing expression of PD-1, T cell immunoglobulin and mucin-domain containing-3 (TIM-3), IFN-γ, TNF, and GrzB. The strongly increased production of IL-4 by tumor-infiltrating CD4$^+$ T_{conv} cells in *Csnk2b*$^{Treg-/-}$ mice (Figure 3B) prompted us to test the effect of exogenous IL-4 in this *in vitro* system. Addition of IL-4 in combination with chronic stimulation resulted in enhanced viability of CTLs (Figure 3H), reduced PD-1 and TIM-3 double-expressing cells (Figure 3I), and enhanced IFN-γ and GrzB expression, while TNF expression was unaffected (Figure 3J). These data strongly suggest that enhanced concentrations of IL-4 are able to prevent exhaustion of CTLs in tumors of *Csnk2b*$^{Treg-/-}$ mice.

Protein kinase CK2 regulates the tissue repair program in T_{reg} cells

Next, we sought to understand the relationships between the lack of CK2β in T_{reg} cells, ILT3$^+$ T_{reg} cell development, and the induction of a type 2 antitumor immune response. Thus, we measured ILT3$^+$ T_{reg} cells in the tumors of *Csnk2b*$^{Treg-/-}$ and *Csnk2b*$^{fl/fl}$ mice by multicolor flow cytometry. These analyses demonstrated that the percentage (Figure 4A) and absolute number (Figure 4B) of tumor-infiltrating ILT3$^+$ T_{reg} cells were significantly increased in *Csnk2b*$^{Treg-/-}$ mice. These findings led us to investigate the signal transduction pathway of polyamine-steered CK2 activity in T_{reg} cells. Hence, we conducted kinome analyses in CK2β-deficient T_{reg} cells and CK2β-competent T_{reg} cells. These analyses demonstrated a strong effect on several downstream pathways of CK2, including Lyn (Figures 4C and S4A; Table S3), a kinase essential for tissue-resident T_{reg} cell (tisT_{reg} cell) development and function.[31] CK2 was shown to regulate nuclear export of peroxisome proliferator-activated receptor gamma (PPARγ),[32] a transcription factor associated with T_{reg} cell tissue residency.[33,34] To analyze the correlation between reduced CK2 activity in CK2β-deficient T_{reg} cells and PPARγ and ILT3 expression, we analyzed the expression of ILT3 in PPARγ-deficient T_{reg} cells. This analysis demonstrated strongly reduced mRNA expression of *Lilrb4a*, the gene encoding for ILT3 (Figure S4B). To determine the relationship between ILT3$^+$ T_{reg} cells and tisT_{reg} cells, we performed RNA-seq on ILT3$^+$ and ILT3$^-$ T_{reg} cells from C57BL/6J mice and compared their expression of tisT_{reg} cell-associated genes, based on data by Feuerer et al.[25,35] (Figure 4D). These comparative analyses demonstrated almost complete concordance between ILT3$^+$ T_{reg} cells and tisT_{reg} cells isolated from skin at the bulk transcriptional level. To confirm ILT3 as a tisT_{reg} cell surface marker, we analyzed expression of ST2, KLRG1, and GATA3 on tumor-infiltrating ILT3$^-$ and ILT3$^+$ T_{reg} cells by multicolor flow cytometry (Figure S4C). This analysis demonstrated an enhanced percentage of ST2, KLRG1, and GATA3 among ILT3$^+$ T_{reg} cells. Furthermore, amphiregulin (AREG) and *Vegfa* expression were greatly enhanced in ILT3$^+$ T_{reg} cells, suggesting tissue reparative properties, especially among these cells (Figures S4D and S4E).

To analyze the tisT_{reg} cell signature in tumor-infiltrating CK2β-deficient T_{reg} cells, we performed flow cytometric analyses to assess the expression of ST2, KLRG1, GATA3, and CD103 on T_{reg} cells isolated from the TME of *Csnk2b*$^{Treg-/-}$ and *Csnk2b*$^{fl/fl}$ mice. These analyses demonstrated high expression of ST2, KLRG1, GATA3, and CD103, in addition to ILT3, on CK2β-deficient T_{reg} cells (Figure 4E).

To investigate the impact of CK2β-deficiency on tissue repair properties, we isolated T_{reg} cells from *Csnk2b*$^{Treg-/-}$ and *Csnk2b*$^{fl/fl}$ mice and stimulated these cells for 72 h to allow for the secretion of wound healing factors. ELISA-based measurements revealed strongly enhanced production of the tisT_{reg} cell effector molecule AREG and vascular endothelial growth factor (VEGF) by CK2β-deficient T_{reg} cells (Figure 4F). To analyze tissue repair function, cell-free supernatant was collected and evaluated in a wound healing assay with 3T3 murine fibroblast cells. Supernatant from CK2β-deficient T_{reg} cells closed cellular gaps faster than controls, suggesting enhanced tissue reparative properties (Figure 4G). To understand the role of CK2β in tisT_{reg} cell development on a genome-wide level, we isolated T_{reg} cells of *Csnk2b*$^{Treg-/-}$ and *Csnk2b*$^{fl/fl}$ mice, stimulated these cells for 72 h by a combination of αCD3 and αCD28, and conducted bulk RNA-seq. This analysis demonstrated strongly enhanced expression of genes associated with the tisT_{reg} cell phenotype, including *Il1rl1*, *Klrg1*, *Itgae*, *Gata3, Areg,* and *Batf* (Figure 4H; Table S5).

Together, these results indicate that polyamine-driven activity of protein kinase CK2 in T_{reg} cells stabilizes suppressive properties and prevents tissue repair functions.

Polyamines steer kinase CK2-regulated tissue reparative properties of T_{reg} cells

To obtain a comprehensive overview of the changes induced by polyamine deprivation and concomitantly reduced CK2 activity, we performed bulk RNA-seq analyses of T_{reg} cells in the presence and absence of DFMO. T_{reg} cells were isolated from splenocytes of C57BL/6J mice using magnetic beads and subsequently cultured in polyamine-free medium with or without DFMO to inhibit intrinsic polyamine synthesis.

The analyses demonstrated enhanced expression of genes associated with reparative properties in tisT_{reg} cells. In particular, a comparatively strong expression of the genes *Klrg1*, *Il1r1*, *Areg*, and *Lilrb4a* was observed after polyamine deprivation (Figure 5A; Table S6). Moreover, analyses of the culture supernatants of these cells revealed strong AREG production, further underlining the induction of tisT_{reg} cell function by polyamine deprivation (Figure 5B).

To confirm that polyamines steer the development of ILT3$^+$ T_{reg} cells, we isolated T_{reg} cells from splenocytes of *Csnk2b*$^{Treg-/-}$ and *Csnk2b*$^{fl/fl}$ mice and conducted bulk RNA-seq upon stimulating the cells in the presence and absence of DFMO. These analyses confirmed that polyamine deprivation

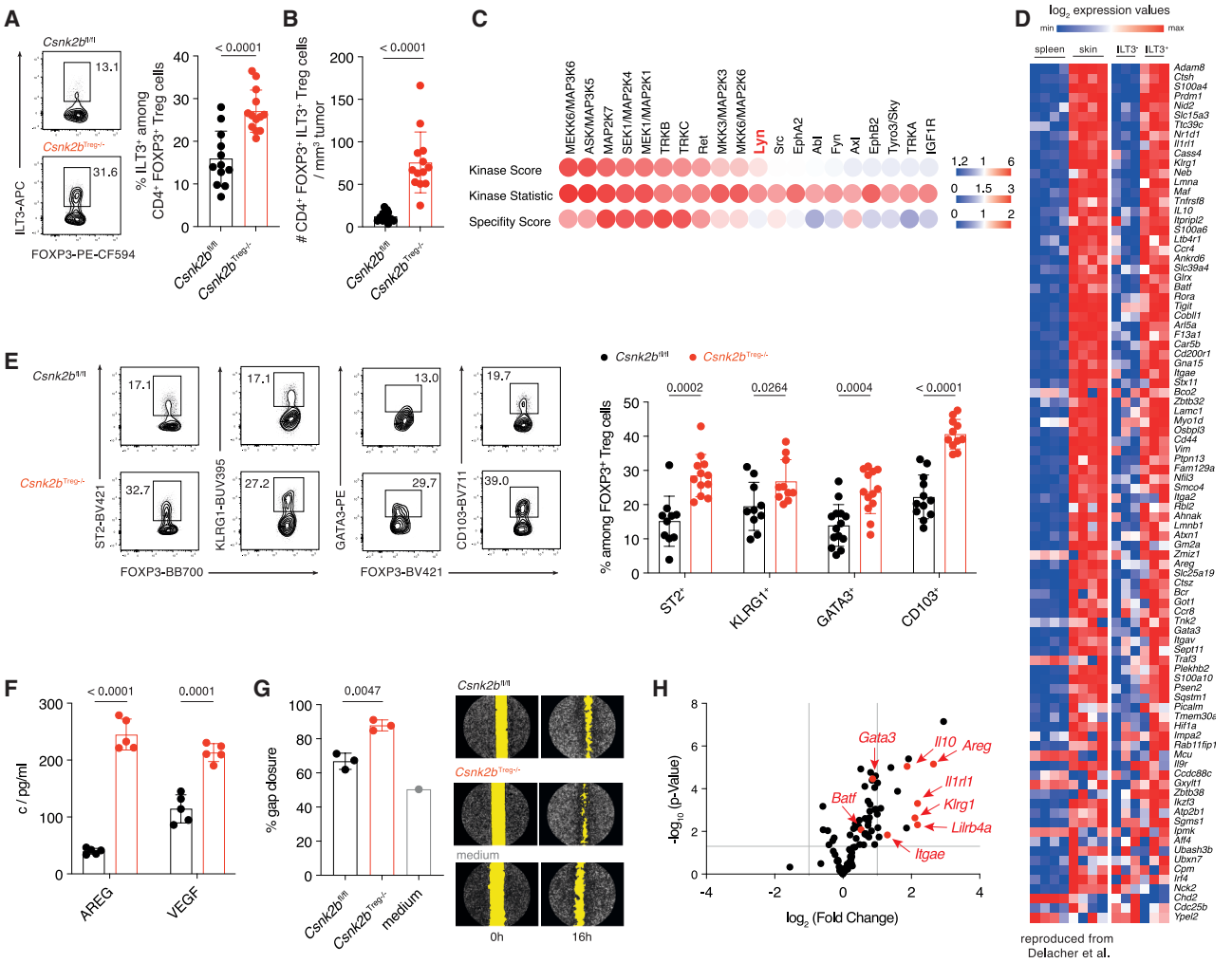

Figure 4. Ck2β-deficient T_{reg} cells show distinct features of tissue repair T_{reg} cells

(A) Representative flow cytometry plots and percentage quantification of ILT3$^+$ T_{reg} cells (ILT3$^+$ among CD45$^+$TCRβ$^+$ CD4$^+$FOXP3$^+$ cells) in tumors of *Csnk2b*$^{fl/fl}$ (n = 12) and *Csnk2b*$^{Treg-/-}$ (n = 13) mice.

(B) Total numbers of life CD45$^+$TCRβ$^+$CD4$^+$FOXP3$^+$ILT3$^+$ T_{reg} cells in tumors (per mm^3 tumor tissue) of *Csnk2b*$^{fl/fl}$ (n = 12) and *Csnk2b*$^{Treg-/-}$ (n = 13) mice.

(C) Kinase activity analysis of the top 20 kinases with increased activity in CK2β-deficient vs. WT T_{reg} cells (n = 6/group; Table S3). The top heatmap shows kinase scores (significant if > 1.2), the middle heatmap displays kinase statistics (>0 = increased activity in CK2β-deficient T_{reg} cells), and the bottom heatmap shows specificity scores.

(D) Expression of tisT_{reg}-associated genes in skin/spleen T_{reg} cells compared with ILT3$^+$ and ILT3$^-$ T_{reg} cells (Table S4).

(E) Representative flow cytometry plots and quantification of ST2$^+$, KLRG1$^+$, GATA3$^+$, and CD103$^+$ T_{reg} cells in tumors of *Csnk2b*$^{fl/fl}$ (ST2: n = 10; KLRG1: n = 10; GATA3: n = 14; CD103: n = 12) and *Csnk2b*$^{Treg-/-}$ mice (ST2: n = 12; KLRG1: n = 10; GATA3: n = 13; CD103: n = 12).

(F) ELISA-based quantification of AREG and VEGF in supernatants of αCD3/28-stimulated WT (*Csnk2b*$^{fl/fl}$) or CK2β-deficient (*Csnk2b*$^{Treg-/-}$) T_{reg} cells (n = 5/group).

(G) Quantification of gap closure in 3T3 cultures exposed to supernatants of WT (*Csnk2b*$^{fl/fl}$) or CK2β-deficient (*Csnk2b*$^{Treg-/-}$) T_{reg} cells (n = 3/group); representative images shown.

(H) mRNA-seq of αCD3/28-stimulated WT and CK2β-deficient T_{reg} cells (n = 5/group). Volcano plot shows tisT_{reg}-related genes (significance: FC > 2, p < 0.05; Table S5). Genes of interest were highlighted in red. Flow cytometry was performed on day 21 post B16.F10 cells injection. Data in box dot plots (A, B, and E–G) are shown as mean ± SD with individual biological replicates plotted. p values were calculated using two-tailed unpaired t tests with Welch's correction. See also Figure S4.

as well as CK2β deficiency results in expression of genes associated with a tisT_{reg} cell phenotype and demonstrated that the expression of 283 genes among 501 polyamine-dependently upregulated genes depends on CK2β (Figure S5A; Table S7).

To further confirm this result on the protein level, we conducted flow cytometric analysis to test for the expression of the tisT_{reg} cell markers ST2, KLRG1, GATA3, and CD103 upon culturing the cells in polyamine-free medium with or without DFMO. This analysis confirmed enhanced expression of these tisT_{reg} cell markers by flow cytometry (Figure 5C) under polyamine deprivation. Polyamine deprivation alone strongly increased the expression of all measured markers of tisT_{reg} cells

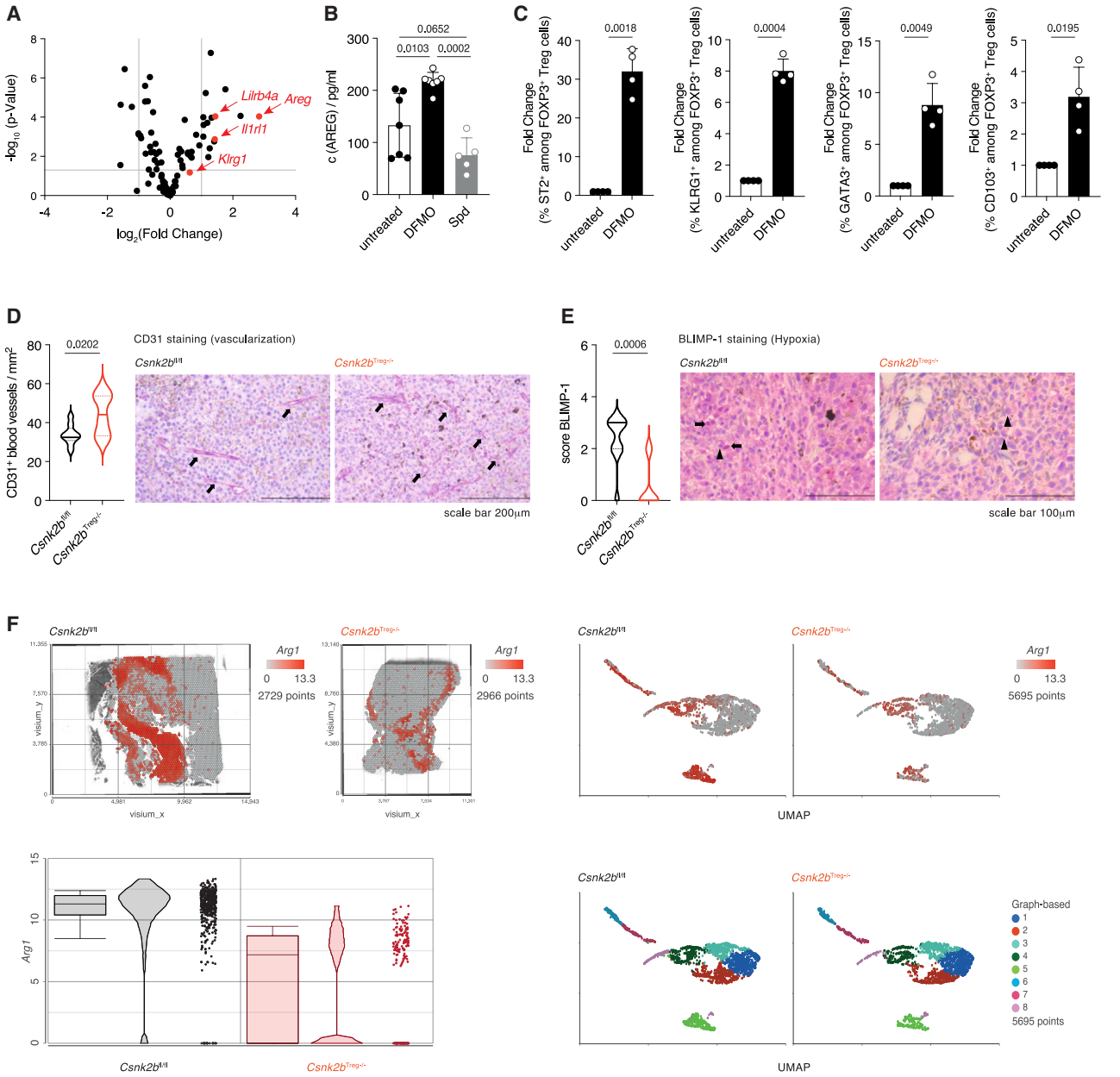

Figure 5. Polyamines modulate the tissue reparative capabilities of T_{reg} cells

(A) mRNA-seq of α-CD3/28-stimulated WT T_{reg} cells ±1 mM DFMO (n = 5/group). Volcano plot shows tisT_{reg}-related genes (significance: FC > 2, $p < 0.05$; Table S6). Genes of interest were highlighted in red.

(B) AREG levels in supernatants of untreated (n = 7) or pretreated (1 mM DFMO [n = 7]; 2.5 µM Spd [n = 5]) T_{reg} cells measured by ELISA.

(C) Fold change of ST2, KLRG1, GATA3, and CD103 expression in DFMO-treated T_{reg} cells (n = 4/group). Fold change of untreated samples (filled circles) was defined as 1.

(D and E) Quantification of CD31$^+$ vessels (per mm^2) (D) and BLIMP-1 staining score (E) in B16.F10 tissue tumor sections of *Csnk2b*$^{fl/fl}$ mice and *Csnk2b*$^{Treg-/-}$ mice (n = 9/group), representative images of CD31-staining (scale bar: 200 µm) and BLIMP-staining (scale bar: 100 µm) are shown.

(F) Representative spatial transcriptomics of B16.F10 tumors from *Csnk2b*$^{fl/fl}$ mice and *Csnk2b*$^{Treg-/-}$ mice. Upper left: *Arg1* expression across tissue sections. Upper right: UMAP showing *Arg1* expression across graph-based clusters. Lower left: violin plot highlighting *Arg1* expression in cluster 5 (tumor-infiltrating macrophages). Lower right: UMAP of unbiased cell-type classification. Tissue sections were collected at day 15 post-s.c. injection of B16.F10 cells. Data in box dot plots (B and C) are shown as mean ± SD with individual biological replicates plotted. Statistical comparisons were performed using two-tailed unpaired t tests with Welch's correction.

See also Figure S5.

only in the presence of CK2β (Figures S5B and S5C). This result further substantiates that polyamine deprivation plays a central role in ILT3$^+$ T_{reg} cell development in a CK2β-dependent manner.

To understand the impact of a tisT_{reg} cell-orchestrated tissue repair program in the TME, we analyzed TME vascularization by immunohistochemistry. Concomitant with increased ILT3$^+$ T_{reg} cell numbers in the TME of *Csnk2b*$^{Treg-/-}$ mice, tumors showed enhanced CD31$^+$ vessel formation (Figure 5D), which might help to reduce hypoxia, improve nutrient supply, and facilitate removal of metabolic byproducts. To examine hypoxia in these tumors, we further stained for the transcription factor B lymphocyte-induced maturation protein-1 (BLIMP-1), whose expression is regulated by hypoxia-inducible factor 1-alpha (HIF1α) and increases under hypoxic conditions.[36] BLIMP-1 expression was significantly reduced in the tumors of *Csnk2b*$^{Treg-/-}$ mice compared with those of *Csnk2b*$^{fl/fl}$ mice (Figure 5E), indicating less hypoxia. To understand the effect of enhanced vascularization in a spatial manner, we conducted spatial transcriptomics of tumor sections. The expression of *Arg1*, shown to be regulated by hypoxia-dependent HIF activity in tumor-associated macrophages,[37] was strongly reduced in tumors of *Csnk2b*$^{Treg-/-}$ mice when compared with tumors grown in *Csnk2b*$^{fl/fl}$ mice (Figure 5F, top). Through clustering and classification, we found that cluster 5, representing tumor-associated macrophages, highly expresses *Arg1* in tumors grown in *Csnk2b*$^{fl/fl}$ mice but not in tumors of *Csnk2b* $^{Treg-/-}$ mice, supporting that the tissue repair properties of CK2β-deficient T_{reg} cells contribute to coordinated vessel formation and reduced hypoxia (Figure 5F, bottom).

In summary, ILT3$^+$ T_{reg} cell-driven tissue repair function might be responsible for enhanced vessel formation, reduced hypoxia, and a strong antitumor immune response in *Csnk2b*$^{Treg-/-}$ mice.

Polyamine metabolism is an attractive target for T_{reg} cell-based tumor therapy

Combinatorial treatment of polyamine transporter inhibitor AMXT 1501 and ODC1 inhibitor DFMO is currently being tested in clinical trials. To understand the impact of this therapeutic approach on T_{reg} cell phenotype and function in the TME of treated tumors, we inoculated *Csnk2b*$^{Treg-/-}$ and *Csnk2b*$^{fl/fl}$ mice with B16.F10 cells and orally administered DFMO in combination with peritumoral s.c. injection of AMXT 1501. We measured tumor growth and analyzed the phenotype of T_{reg} cells in the TME by multicolor flow cytometry. Combinatorial treatment had no effect on tumor growth in *Csnk2b*$^{Treg-/-}$ mice but strongly attenuated tumor growth in *Csnk2b*$^{fl/fl}$ mice, which showed growth comparable to the retarded tumor growth seen in both treated and untreated *Csnk2b*$^{Treg-/-}$ mice (Figure 6A). Furthermore, this treatment had no effect on overall T_{reg} cells in the TME (Figure 6B), but strongly enhanced the development of ILT3$^+$ T_{reg} cells in percentage (Figure 6C) and in total numbers (Figure S6A), reaching levels comparable to *Csnk2b*$^{Treg-/-}$ mice. Concomitantly, this treatment resulted in enhanced type 2 antitumor immunity, evidenced by increased percentage (Figures 6D–6F) and total numbers (Figures S6B–S6D) of GATA3- (Figure 6D), IL-4- (Figure 6E), and IL-13- (Figure 6F) expressing tumor-infiltrating T_{conv} cells without changing the percentage of IFN-γ expressing T_{conv} cells (Figure 6G). Together, these results indicate that tumor-derived polyamines control the ILT3$^+$ T_{reg} cell development and that polyamine deprivation induces efficient type 2 antitumor immunity in an ILT3$^+$ T_{reg} cell- and CK2β-dependent manner *in vivo*.

ILT3$^+$ T_{reg} cells and type 2 antitumor immune responses are beneficial for melanoma patients

To understand whether reduced CK2 expression or enhanced expression of *LILRB4* (the gene encoding for ILT3) in T_{reg} cells shows a survival benefit for melanoma patients, we employed bioinformatic analysis using TCGA data. Consistent with our preclinical model data, decreased expression of *CSNK2B* in combination with a T_{reg} cell transcriptomic signature (low *CSNK2B* expression/high T_{reg} cells), as well as increased expression of *LILRB4* in combination with a T_{reg} cell transcriptomic signature (high *LILRB4* expression/high T_{reg} cells) in tumor biopsies, was significantly associated with prolonged survival in melanoma patients (Figures 7A and 7B). Likewise, decreased expression of *CSNK2B* and enhanced expression of the T_H2 cell master transcription factor *GATA3* or of *SIGLEC8*, a molecule strongly expressed by eosinophils, were also associated with prolonged survival (Figures S7A–S7C). Moreover, ILT3 expression was positively correlated with the expression of *GATA3* and *SIGLEC8* in tumor biopsies (Figures S7D and S7E). To understand the role of CK2β in T_{reg} cells and the role of ILT3$^+$ T_{reg} cells in patient tumors, we extracted a gene signature specific for these cells from RNA-seq analysis (*Areg*, *Batf*, *Ccr8*, *Cd44*, *Gata3*, *Gzmb*, *Il10*, *Il1rl1*, *Irf4*, *Itgae*, *Klrg1*, and *Lilrb4a*) and used this transcriptomic signature for survival rate analyses with TCGA datasets. These analyses showed that enhanced expression of this T_{reg} cell transcriptomic signature resulted in an improved survival rate (Figure S7F). Hence, these analyses support that ILT3$^+$ T_{reg} cells play an important role in orchestrating efficient T_H2 cell-driven type 2 antitumor immunity in humans.

Finally, to test the therapeutic potential of the identified pathway for the treatment of melanomas, we s.c. inoculated *Csnk2b*$^{Treg-/-}$ and *Csnk2b*$^{fl/fl}$ mice with B16.F10 cells. Upon palpability of tumors at day 7 after inoculation, we s.c. injected a CK2 inhibitor (2-dimethylamino-4,5,6,7-tetrabromo-1H-benzimidazole; DMAT) at a dose of 10 mg/kg body weight and monitored subsequent tumor growth. This treatment had no effect on the differentiation of T_H2 cells themselves (Figure S7G) and no activating effect on CTLs (Figure S7H) but resulted in strong inhibition of tumor growth in *Csnk2b*$^{fl/fl}$ mice, comparable to that observed in treated or untreated *Csnk2b*$^{Treg-/-}$ mice (Figure 7C). Multicolor flow cytometry revealed that the strongly reduced tumor growth after DMAT treatment was accompanied by an increased percentage of ILT3$^+$ T_{reg} cells in the TME (Figure 7D). Comparative analysis of the transcriptomes of DMAT-treated and untreated CK2β-deficient T_{reg} cells revealed hardly any DEGs, demonstrating specificity for CK2 inhibition at the concentration used (data not shown).

In summary, these results demonstrate the crucial role of polyamine-steered CK2 activity for the development and function of ILT3$^+$ T_{reg} cells that orchestrate effective type 2 antitumor immunity and maintain immune homeostasis.

DISCUSSION

Despite extensive research, selectively modulating T_{reg} functions involved in immune suppression in tumors without impairing their

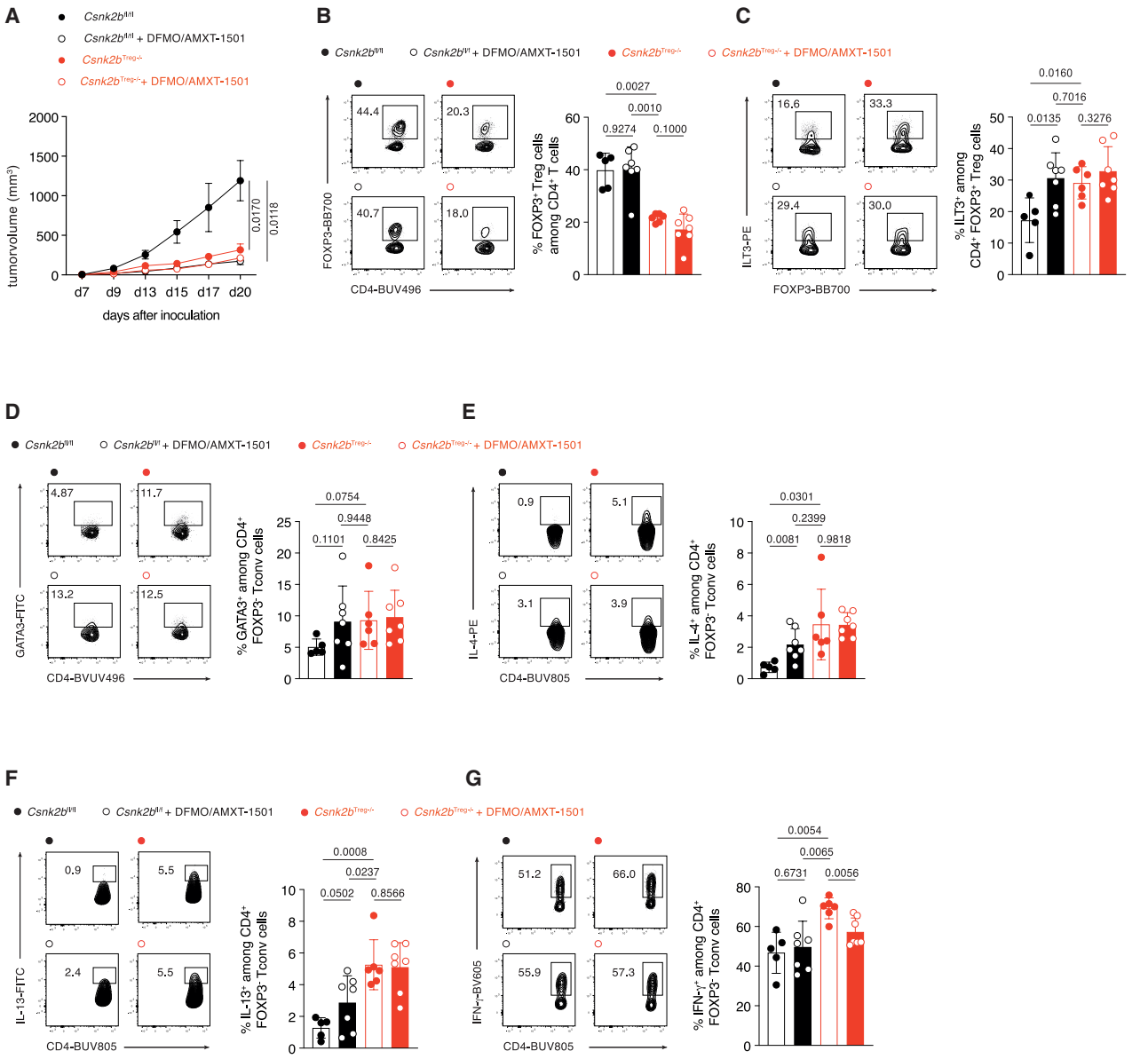

Figure 6. Tumor-derived polyamines alter intra-tumoral T_{reg} cell phenotype, hindering effective antitumor responses

(A) Tumor growth kinetics of B16.F10 tumors in *Csnk2b*$^{fl/fl}$ mice and *Csnk2b*$^{Treg-/-}$ mice treated with DFMO (1% w/v in drinking water) and AMXT-1501 (3 mg/kg body weight intraperitoneally [i.p.]) (n = 7/group) or left untreated (n = 6/group). Shown p values indicate significant differences between untreated *Csnk2b*$^{fl/fl}$ (*Csnk2b*$^{fl/fl}$) and DFMO/AMXT-1501-treated *Csnk2b*$^{fl/fl}$ mice (*Csnk2b*$^{fl/fl}$ + DFMO/AMXT-1501) and untreated *Csnk2b*$^{Treg-/-}$ (*Csnk2b*$^{Treg-/-}$) mice.

(B and C) Representative flow cytometry plots and percentage quantification of FOXP3$^+$ T_{reg} cells and ILT3$^+$ T_{reg} cells in tumors of untreated (filled circles) and DFMO/AMXT-1501-treated (open circles) *Csnk2b*$^{fl/fl}$ and *Csnk2b*$^{Treg-/-}$ mice (*Csnk2b*$^{fl/fl}$ n = 5; *Csnk2b*$^{fl/fl}$ + DFMO/AMXT-1501 n = 7; *Csnk2b*$^{Treg-/-}$ n = 6; *Csnk2b*$^{Treg-/-}$ + DFMO/AMXT-1501 n = 7).

(D–G) Representative flow cytometry plots and quantification of GATA3$^+$ (D), IL-4$^+$ (E), IL-13$^+$ (F), and IFN-γ$^+$ (G) CD4$^+$ T_{conv} in tumors of untreated (filled circles) and DFMO/AMXT-1501-treated (open circles) *Csnk2b*$^{fl/fl}$ and *Csnk2b*$^{Treg-/-}$ mice (*Csnk2b*$^{fl/fl}$ n = 5; *Csnk2b*$^{fl/fl}$ + DFMO/AMXT-1501 n = 7; *Csnk2b*$^{Treg-/-}$ n = 6; *Csnk2b*$^{Treg-/-}$ + DFMO/AMXT-1501 n = 7). Flow cytometry was performed on day 20 post B16.F10 cell injection. Tumor growth (A) is shown as mean ± SEM. Data in box dot plots (B–G) are shown as mean ± SD with individual biological replicates plotted. Statistical significance was assessed using two-tailed unpaired t tests with Welch's correction. p values are indicated in the figures.

See also Figure S6.

role in tissue homeostasis and autoimmunity remains challenging. Due to their dual role in maintaining tolerance and promoting tumor progression, most T_{reg} cell-targeted therapies risk inducing autoimmune side effects by affecting T_{reg} cells indiscriminately.

Our study demonstrates that distinct T_{reg} cell functions can be modulated separately. Inhibiting ODC1-dependent polyamine synthesis in tumor cells reshaped the TME, leading to reduced tumor growth, increased IL-4$^+$ and IFN-γ$^+$ T cell

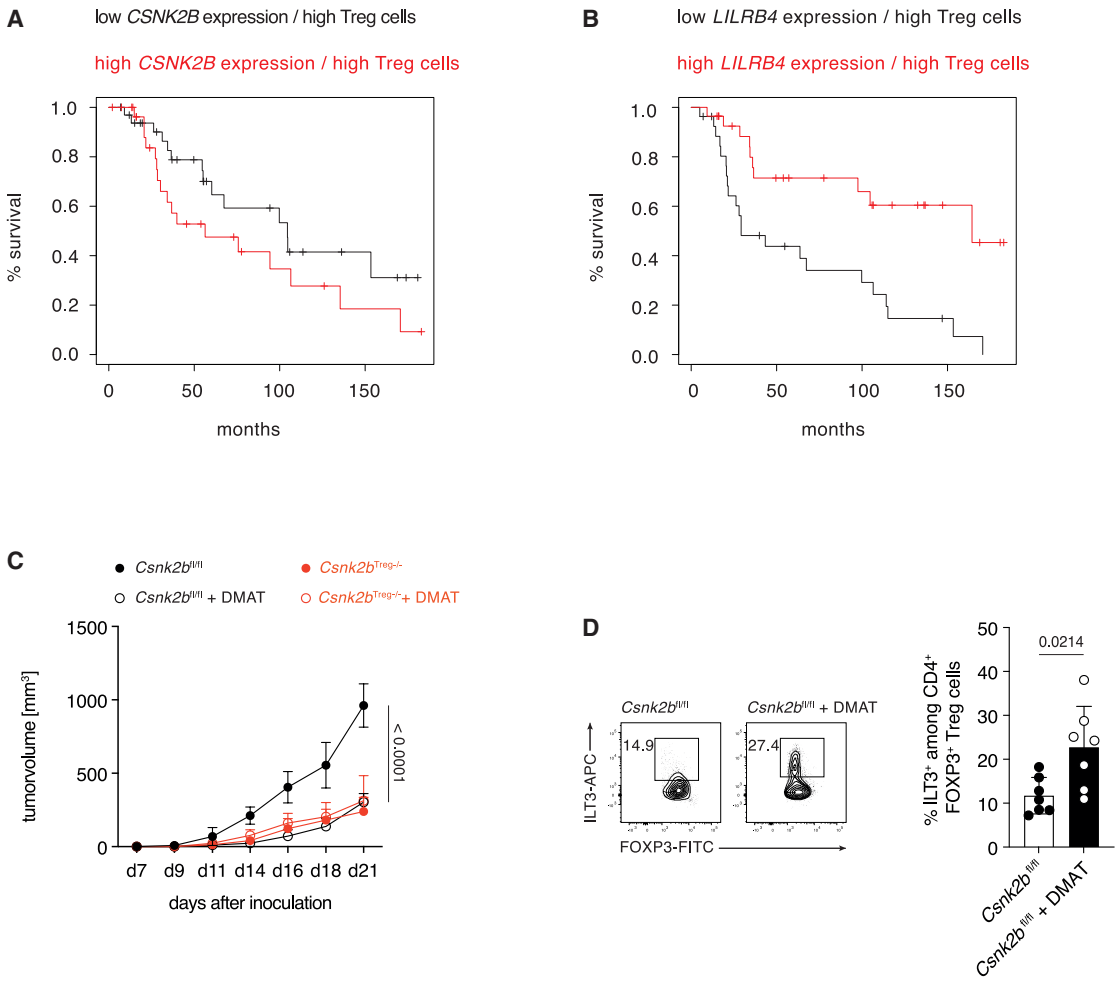

Figure 7. Loss of *Csnk2b* or pharmacological CK2 inhibition reprograms tumor-infiltrating T_{reg} cells and is associated with suppressed melanoma growth and enhanced patient survival

(A and B) Kaplan-Meier survival curves for SKCM patients (n = 343) with high vs. low expression of *CSNK2B* (A) or *LILRB4* (B) and high T_{reg} cell signature (cutoff: 70% vs. 30%); analysis via TIMER2.0 (CIBERSORT algorithm).

(C) Tumor growth kinetics of B16.F10 tumors in *Csnk2b*$^{fl/fl}$ mice and *Csnk2b*$^{Treg-/-}$ mice treated with DMAT (10 mg/kg body weight s.c. injected on days 9, 11, 14, 17, and 20) or left untreated (n = 7/group). Shown p values indicate significant differences between untreated *Csnk2b*$^{fl/fl}$ (*Csnk2b*$^{fl/fl}$) and DMAT-treated *Csnk2b*$^{fl/fl}$ mice (*Csnk2b*$^{fl/fl}$ + DMAT).

(D) Representative flow cytometry plots and quantification of ILT3$^+$ T_{reg} cells in tumors of untreated (filled circles) and DMAT-treated (open circles) *Csnk2b*$^{fl/fl}$ mice (n = 7 per group). Flow cytometry was performed on day 21 post B16.F10 cell injection. Tumor growth (C) is shown as mean ± SEM. Data in box dot plots (D) are shown as mean ± SD with individual biological replicates plotted. Statistical significance was assessed using two-tailed unpaired t tests with Welch's correction. p values are indicated in the figures.

See also Figure S7.

infiltration, and notably, the accumulation of ILT3$^+$ T_{reg} cells. These ILT3$^+$ T_{reg} cells resemble CCR8$^+$ tisT_{reg} cells, characterized by tissue repair functions in both healthy and tumor tissues.

Functionally, ILT3$^+$ T_{reg} cells support antitumor immunity and promote beneficial neoangiogenesis by enhancing type 2 immune responses, thereby reducing hypoxia in the TME. At the same time, they retain the capacity to suppress T_H1/T_H17-driven autoimmunity. Similar to conventional FOXP3$^+$ T_{reg} cells, ILT3$^+$ T_{reg} cells effectively control T_H1 activity *in vitro* and *in vivo*, suppress T_H1-mediated colitis, and prevent the induction of experimental autoimmune encephalomyelitis (EAE). Since polyamines modulate CK2 activity in T_{reg} cells, both CK2β-deletion and polyamine blockade via DFMO and AMXT-1501 led to comparable ILT3$^+$ T_{reg} cell expansion and function.

Our analyses confirmed that both polyamine deprivation and CK2β deficiency induce gene expression linked to the tisT_{reg} cell phenotype. Moreover, expression of 283 out of 501 polyamine-dependent genes required the presence of CK2β.

Our findings also highlight CK2-independent roles of polyamines in key cellular processes. Nonetheless, the data underscore the therapeutic potential of targeting polyamine synthesis or polyamine-mediated regulation of CK2 activity.

Expansion of ILT3$^+$ T_{reg} cells promoted type 2 immunity and correlated with improved survival in melanoma patients. This response was accompanied by increased numbers of CTLs producing IFN-γ and TNF-α, reduced expression of exhaustion markers PD-1 and LAG-3, and enhanced eosinophil infiltration, explaining the reduced tumor growth. Consistent with findings by Bing Feng et al.,[38] our data support a role for IL-4 in enhancing CD8$^+$ T cell fitness within the TME. These results might explain why tumor control was achieved by either CK2β deletion in T_{reg} cells or pharmacological CK2 inhibition via DMAT, both of which counteracted polyamine-driven immunosuppression.

Polyamines are essential for cell growth and accumulate in rapidly proliferating tissues. Tumor cells significantly contribute to elevated polyamine levels in cancer patients with direct crosstalk between polyamine metabolism and oncogenic pathways such as MYC, PTEN-phosphatidylinositol 3-kinase (PI3K)-mTORC1, WNT, and RAS, which enhance ODC1 expression and activity.[39–41] In turn, polyamines promote proliferation by supporting DNA synthesis and stability, transcriptional regulation, ion channel function, and protein phosphorylation.[42]

Beyond their role in tumor cell proliferation, polyamines shape a tumor-permissive microenvironment by modulating immune cell recruitment and function. They drive immunosuppression by promoting alternatively activated macrophages via IL-33,[43] inhibiting lymphocyte proliferation and IL-2 production, and impairing natural killer (NK) cell activity.[44] Additionally, they support myeloid cell-driven immunosuppression in glioblastoma.[45] These findings are in line with observations showing that blocking polyamine production reestablished the T cell-dependent control of tumor growth.[44]

We raise the question of how polyamines influence T_{reg} cell identity and ILT3$^+$ T_{reg} cell development. We propose a model in which polyamines modulate ILT3$^+$ T_{reg} cell development by affecting CK2 activity[46] and downstream PPARγ signaling. Polyamines have been shown to increase CK2α/β expression, and CK2-mediated phosphorylation of PPARγ leads to its nuclear export.[32] Since PPARγ, essential for non-lymphoid T_{reg} cell function,[34] has predicted binding sites in the *LILRB4* locus, its nuclear exclusion may suppress ILT3 expression. This is supported by our finding that *Lilrb4a* is downregulated in PPARγ-deficient T_{reg} cells. Thus, high polyamine levels could reduce nuclear PPARγ and inhibit ILT3$^+$ T_{reg} cell development, while polyamine depletion or CK2 inhibition may promote ILT3 expression and type 2 immunity. Whether this pathway similarly regulates T_{reg} cells in other tissues remains to be investigated. Furthermore, enhanced vascularization in tumors of *Csnk2b*$^{Treg-/-}$ mice may contribute to improved antitumor immunity by reducing hypoxia and supporting immune cell function.

Our findings reveal that polyamines regulate CK2 activity in T_{reg} cells, with significant effects on their phenotype and function—balancing tumor immune control and immune tolerance. Improved survival in patients with low CSNK2B or high LILRB4 expression supports a beneficial role for ILT3$^+$ T_{reg} cells in human melanoma. We therefore propose the ILT3$^+$/ILT3$^-$FOXP3$^+$ T_{reg} cell ratio as a more informative prognostic marker than total FOXP3$^+$ T_{reg} numbers. Whether this applies across tumor types remains to be determined. Importantly, our data support the rationale for targeting polyamine synthesis or function in combination with immune checkpoint inhibitors (ICIs), which rely on effective CTL responses. Modulating the polyamine-driven immunosuppressive microenvironment could enhance the efficacy of ICI therapies in melanoma and beyond.

Limitations of the study

While our findings suggest a role for IL-4 and other type 2 cytokines in the ILT3$^+$ tisT_{reg} cell-mediated revitalization of CTLs, further experiments using conditional *Il4* or *Il4ra* deletion mouse models are necessary to conclusively establish this relationship. Additionally, our investigation of polyamine effects on T_{reg} cells focused primarily on CK2β-binding, but polyamines may impact these cells also through other mechanisms that were not explored in this study. The use of *Odc1* germline deletion in tumors to prevent polyamine production exclusively may not account for alternative ODC1-independent polyamine production pathways. Furthermore, while we observed specific effects on T_{reg} cells in the TME of melanomas, it remains to be determined whether this mechanism controls the phenotype and function of tisT_{reg} cells in other tissues. These limitations highlight the need for further research to fully elucidate the complex interactions between polyamines, CK2, and tisT_{reg} cell function in various contexts.

RESOURCE AVAILABILITY

Lead contact

Further information and requests for resources and reagents should be directed to and will be fulfilled by the lead contact, Tobias Bopp (boppt@uni-mainz.de).

Materials availability

The study did not generate new, unique reagents and materials. Reagents used in this study are available from the lead contact upon reasonable request.

Data and code availability

- The metabolomics data have been deposited to MetaboLights[47] repository. The study identifier is listed in the key resources table.
- mRNA-seq data have been deposited at GEO and are publicly available as of the date of publication. Accession numbers are listed in the key resources table.
- scRNA-seq data have been deposited at GEO and are publicly available as of the date of publication. Accession numbers are listed in the key resources table.
- Spatial transcriptomics data have been deposited at GEO and are publicly available as of the date of publication. Accession numbers are listed in the key resources table.
- This paper does not report original code.
- Any additional information required to reanalyze the data reported in this paper is available from the lead contact upon reasonable request.

ACKNOWLEDGMENTS

We would like to thank S. Fischer and S. Hesse-Kerolli for expert technical help. We are grateful to M. Diken (Translational Oncology [TRON] at the University Medical Center of the Johannes Gutenberg University gGmbH, Mainz) for providing B16.F10 melanoma cells and HC Probst for providing MC38 adenocarcinoma cells. This work was supported by the Deutsche Forschungsgemeinschaft (D.F.G.) project-ID 318346496/SFB 1292 TP01 (T. Bopp), TP13 (H.S. and H.C.P.), TP19 (M.D.), TP22 (M.M.G.), and TPQ1 (M.M.G.); SFB 1066 project B04 (H.S.), B13 (T. Bopp), B8 (T. Bopp), SFB TRR 156 B02 (H.C.P. and H.S.), B11 (T. Bopp), project-ID 490846870/SFB TRR 355 A01 (M.D.), A09 (T. Bopp), A10 (T. Bopp), and Z02 (M.D.); "Universitäres Centrum für Tumorerkrankungen (UCT)"; and the "Forschungszentrum Immuntherapie (FZI)" of the University Medical Center. This study was supported by a

research grant of the University Medical Center Giessen and Marburg (UKGM, grant number 09/2023 MR, to A.J.R.O.). I.D. was supported by the Clusterproject ENABLE, funded by the Hessian Ministry for Science and the Arts (HMWK). The graphical abstract and Figure S1C were created in BioRender (https://biorender.com/).

AUTHOR CONTRIBUTIONS

G.B.: data curation, investigation, methodology, visualization, writing – original draft, and writing – review and editing – preparation; A.U.: investigation; J.P.: investigation; N.T.-A.: investigation; M.K.: formal analysis; K.R.: investigation; F.S.: investigation and formal analysis; M.H.: investigation; J.G.S.: formal analysis; L.Z.: formal analysis; L.S.: resources; H.C.P.: resources; U.D.: investigation and formal analysis; S.T.: resources; M.L.: resources; A.J.R.-O.: investigation; H.M.: resources, T. Bohn: investigation; M.D.: resources; T.S.: resources and formal analysis; M.M.G.: investigation and formal analysis; I.D.: writing – review and editing – preparation; C.I.: resources and formal analysis; H.S.: conceptualization, writing – original draft, and writing – review and editing – preparation; T. Bopp: conceptualization, funding acquisition, methodology, resources, supervision, validation, writing – original draft, and writing – review and editing – preparation.

DECLARATION OF INTERESTS

The authors declare no competing interests.

STAR★METHODS

Detailed methods are provided in the online version of this paper and include the following:

- KEY RESOURCES TABLE
- EXPERIMENTAL MODEL AND STUDY PARTICIPANT DETAILS
  - Mice
  - Cell lines and cell culture
- METHOD DETAILS
  - Biogenic amines profiling by mass spectrometry
  - Total Polyamine Assay
  - B16.F10 cell metabolome analysis
  - Subcutaneous tumor mouse models
  - Tumor dissociation for single-cell suspension
  - Isolation of tumor-infiltrating lymphocytes
  - Flow cytometric analysis
  - Magnetic Cell Isolation (MACS)
  - Culture of *ex vivo* $CD4^+$ $CD25^+$ cells
  - Enzyme-linked immunosorbent assay (ELISA)
  - Wound healing assay
  - CK2 kinase activity assay
  - Kinase activity profiling
  - mRNA sequencing
  - Single cell mRNA Sequencing
  - Chronic *in vitro* exhaustion model
  - Spatial Transcriptomics
  - TCGA dataset analysis
  - Docking analysis
  - Immunohistochemistry
  - qPCR analysis
  - Generation of mixed-BM chimeras
  - Mouse model of adoptive-transfer colitis
  - T helper cell polarization
  - $CD8^+$ T cell culture
  - Suppression assays
- QUANTIFICATION AND STATISTICAL ANALYSIS

SUPPLEMENTAL INFORMATION

Supplemental information can be found online at https://doi.org/10.1016/j.immuni.2025.07.007.

Received: April 4, 2024
Revised: January 27, 2025
Accepted: July 9, 2025
Published: July 31, 2025

REFERENCES

1. Murray-Stewart, T.R., Woster, P.M., and Casero, R.A. (2016). Targeting polyamine metabolism for cancer therapy and prevention. Biochem. J. *473*, 2937–2953. https://doi.org/10.1042/BCJ20160383.
2. Martins, V.C., Busch, K., Juraeva, D., Blum, C., Ludwig, C., Rasche, V., Lasitschka, F., Mastitsky, S.E., Brors, B., Hielscher, T., et al. (2014). Cell competition is a tumour suppressor mechanism in the thymus. Nature *509*, 465–470. https://doi.org/10.1038/nature13317.
3. Kanda, H., and Igaki, T. (2020). Mechanism of tumor-suppressive cell competition in flies. Cancer Sci. *111*, 3409–3415. https://doi.org/10.1111/cas.14575.
4. Parker, T.M., Gupta, K., Palma, A.M., Yekelchyk, M., Fisher, P.B., Grossman, S.R., Won, K.J., Madan, E., Moreno, E., and Gogna, R. (2021). Cell competition in intratumoral and tumor microenvironment interactions. EMBO J. *40*, e107271. https://doi.org/10.15252/embj.2020107271.
5. Russell, D.H. (1971). Increased Polyamine Concentrations in the Urine of Human Cancer Patients. Nat. New Biol. *233*, 144–145. https://doi.org/10.1038/newbio233144a0.
6. Pegg, A.E., and Casero, R.A. (2011). Current status of the polyamine research field. Methods Mol. Biol. *720*, 3–35. https://doi.org/10.1007/978-1-61779-034-8_1.
7. Terui, Y., Yoshida, T., Sakamoto, A., Saito, D., Oshima, T., Kawazoe, M., Yokoyama, S., Igarashi, K., and Kashiwagi, K. (2018). Polyamines protect nucleic acids against depurination. Int. J. Biochem. Cell Biol. *99*, 147–153. https://doi.org/10.1016/j.biocel.2018.04.008.
8. Cochet, C., and Chambaz, E.M. (1983). Polyamine-mediated protein phosphorylations: A possible target for intracellular polyamine action. Mol. Cell. Endocrinol. *30*, 247–266. https://doi.org/10.1016/0303-7207(83)90062-x.
9. Filhol, O., Cochet, C., Delagoutte, T., and Chambaz, E.M. (1991). Polyamine binding activity of casein kinase II. Biochem. Biophys. Res. Commun. *180*, 945–952. https://doi.org/10.1016/s0006-291x(05)81157-x.
10. Chantalat, L., Leroy, D., Filhol, O., Nueda, A., Benitez, M.J., Chambaz, E.M., Cochet, C., and Dideberg, O. (1999). Crystal structure of the human protein kinase CK2 regulatory subunit reveals its zinc finger-mediated dimerization. EMBO J. *18*, 2930–2940. https://doi.org/10.1093/emboj/18.11.2930.
11. Leroy, D., Schmid, N., Behr, J.P., Filhol, O., Pares, S., Garin, J., Bourgarit, J.J., Chambaz, E.M., and Cochet, C. (1995). Direct Identification of a Polyamine Binding Domain on the Regulatory Subunit of the Protein Kinase Casein Kinase 2 by Photoaffinity Labeling. J. Biol. Chem. *270*, 17400–17406. https://doi.org/10.1074/jbc.270.29.17400.
12. Leroy, D., Filhol, O., Delcros, J.G., Pares, S., Chambaz, E.M., and Cochet, C. (1997). Chemical features of the protein kinase CK2 polyamine binding site. Biochemistry *36*, 1242–1250. https://doi.org/10.1021/bi961949u.
13. Stark, F., Pfannstiel, J., Klaiber, I., and Raabe, T. (2011). Protein kinase CK2 links polyamine metabolism to MAPK signalling in Drosophila. Cell. Signal. *23*, 876–882. https://doi.org/10.1016/j.cellsig.2011.01.013.
14. Zhang, K., Zakeri, A., Alban, T., Dong, J., Ta, H.M., Zalavadia, A.H., Branicky, A., Zhao, H., Juric, I., Husich, H., et al. (2024). VISTA promotes the metabolism and differentiation of myeloid-derived suppressor cells by STAT3 and polyamine-dependent mechanisms. Cell Rep. *43*, 113661. https://doi.org/10.1016/j.celrep.2023.113661.
15. Ao, Y., Zhang, J., Liu, Z., Qian, M., Li, Y., Wu, Z., Sun, P., Wu, J., Bei, W., Wen, J., et al. (2019). Lamin A buffers CK2 kinase activity to modulate aging in a progeria mouse model. Sci. Adv. *5*, eaav5078. https://doi.org/10.1126/sciadv.aav5078.

16. Wagner, A., Wang, C., Fessler, J., DeTomaso, D., Avila-Pacheco, J., Kaminski, J., Zaghouani, S., Christian, E., Thakore, P., Schellhaass, B., et al. (2021). Metabolic modeling of single Th17 cells reveals regulators of autoimmunity. Cell *184*, 4168–4185. https://doi.org/10.1016/j.cell.2021.05.045.

17. Ulges, A., Klein, M., Reuter, S., Gerlitzki, B., Hoffmann, M., Grebe, N., Staudt, V., Stergiou, N., Bohn, T., Brühl, T.-J., et al. (2015). Protein kinase CK2 enables regulatory T cells to suppress excessive TH2 responses in vivo. Nat. Immunol. *16*, 267–275. https://doi.org/10.1038/ni.3083.

18. Josefowicz, S.Z., Lu, L.-F., and Rudensky, A.Y. (2012). Regulatory T Cells: Mechanisms of Differentiation and Function. Annu. Rev. Immunol. *30*, 531–564. https://doi.org/10.1146/annurev.immunol.25.022106.141623.

19. Panduro, M., Benoist, C., and Mathis, D. (2016). Tissue Tregs. Annu. Rev. Immunol. *34*, 609–633. https://doi.org/10.1146/annurev-immunol-032712-095948.

20. Kryczek, I., Wang, L., Wu, K., Li, W., Zhao, E., Cui, T., Wei, S., Liu, Y., Wang, Y., Vatan, L., et al. (2016). Inflammatory regulatory T cells in the microenvironments of ulcerative colitis and colon carcinoma. OncoImmunology *5*, e1105430. https://doi.org/10.1080/2162402X.2015.1105430.

21. Kryczek, I., Wu, K., Zhao, E., Wei, S., Vatan, L., Szeliga, W., Huang, E., Greenson, J., Chang, A., Roliński, J., et al. (2011). IL-17+ Regulatory T Cells in the Microenvironments of Chronic Inflammation and Cancer. J. Immunol. *186*, 4388–4395. https://doi.org/10.4049/jimmunol.1003251.

22. Togashi, Y., Shitara, K., and Nishikawa, H. (2019). Regulatory T cells in cancer immunosuppression — implications for anticancer therapy. Nat. Rev. Clin. Oncol. *16*, 356–371. https://doi.org/10.1038/s41571-019-0175-7.

23. Sharabi, A., Tsokos, M.G., Ding, Y., Malek, T.R., Klatzmann, D., and Tsokos, G.C. (2018). Regulatory T cells in the treatment of disease. Nat. Rev. Drug Discov. *17*, 823–844. https://doi.org/10.1038/nrd.2018.148.

24. Watson, M.J., Vignali, P.D.A., Mullett, S.J., Overacre-Delgoffe, A.E., Peralta, R.M., Grebinoski, S., Menk, A.V., Rittenhouse, N.L., DePeaux, K., Whetstone, R.D., et al. (2021). Metabolic support of tumour-infiltrating regulatory T cells by lactic acid. Nature *591*, 645–651. https://doi.org/10.1038/s41586-020-03045-2.

25. Delacher, M., Schmidl, C., Herzig, Y., Breloer, M., Hartmann, W., Brunk, F., Kägebein, D., Träger, U., Hofer, A.-C., Bittner, S., et al. (2019). Rbpj expression in regulatory T cells is critical for restraining TH2 responses. Nat. Commun. *10*, 1621. https://doi.org/10.1038/s41467-019-09276-w.

26. Leroy, D., Heriché, J.K., Filhol, O., Chambaz, E.M., and Cochet, C. (1997). Binding of Polyamines to an Autonomous Domain of the Regulatory Subunit of Protein Kinase CK2 Induces a Conformational Change in the Holoenzyme. A PROPOSED ROLE FOR THE KINASE STIMULATION. J. Biol. Chem. *272*, 20820–20827. https://doi.org/10.1074/jbc.272.33.20820.

27. Pettersen, E.F., Goddard, T.D., Huang, C.C., Couch, G.S., Greenblatt, D.M., Meng, E.C., and Ferrin, T.E. (2004). UCSF Chimera—A visualization system for exploratory research and analysis. J. Comput. Chem. *25*, 1605–1612. https://doi.org/10.1002/jcc.20084.

28. Carretero, R., Sektioglu, I.M., Garbi, N., Salgado, O.C., Beckhove, P., and Hämmerling, G.J. (2015). Eosinophils orchestrate cancer rejection by normalizing tumor vessels and enhancing infiltration of CD8(+) T cells. Nat. Immunol. *16*, 609–617. https://doi.org/10.1038/ni.3159.

29. Blank, C.U., Haining, W.N., Held, W., Hogan, P.G., Kallies, A., Lugli, E., Lynn, R.C., Philip, M., Rao, A., Restifo, N.P., et al. (2019). Defining 'T cell exhaustion'. Nat. Rev. Immunol. *19*, 665–674. https://doi.org/10.1038/s41577-019-0221-9.

30. Belk, J.A., Yao, W., Ly, N., Freitas, K.A., Chen, Y.-T., Shi, Q., Valencia, A.M., Shifrut, E., Kale, N., Yost, K.E., et al. (2022). Genome-wide CRISPR screens of T cell exhaustion identify chromatin remodeling factors that limit T cell persistence. Cancer Cell *40*, 768–786. https://doi.org/10.1016/j.ccell.2022.06.001.

31. Spath, S., Roan, F., Presnell, S.R., Höllbacher, B., and Ziegler, S.F. (2022). Profiling of Tregs across tissues reveals plasticity in ST2 expression and hierarchies in tissue-specific phenotypes. iScience *25*, 104998. https://doi.org/10.1016/j.isci.2022.104998.

32. von Knethen, A., Tzieply, N., Jennewein, C., and Brüne, B. (2010). Casein-kinase-II-dependent phosphorylation of PPARgamma provokes CRM1-mediated shuttling of PPARgamma from the nucleus to the cytosol. J. Cell Sci. *123*, 192–201. https://doi.org/10.1242/jcs.055475.

33. Cipolletta, D., Feuerer, M., Li, A., Kamei, N., Lee, J., Shoelson, S.E., Benoist, C., and Mathis, D. (2012). PPAR-γ is a major driver of the accumulation and phenotype of adipose tissue Treg cells. Nature *486*, 549–553. https://doi.org/10.1038/nature11132.

34. Li, C., Muñoz-Rojas, A.R., Wang, G., Mann, A.O., Benoist, C., and Mathis, D. (2021). PPARγ marks splenic precursors of multiple nonlymphoid-tissue Treg compartments. Proc. Natl. Acad. Sci. USA *118*, e2025197118. https://doi.org/10.1073/pnas.2025197118.

35. Delacher, M., Imbusch, C.D., Weichenhan, D., Breiling, A., Hotz-Wagenblatt, A., Träger, U., Hofer, A.-C., Kägebein, D., Wang, Q., Frauhammer, F., et al. (2017). Genome-wide DNA-methylation landscape defines specialization of regulatory T cells in tissues. Nat. Immunol. *18*, 1160–1172. https://doi.org/10.1038/ni.3799.

36. Chiou, S.-H., Risca, V.I., Wang, G.X., Yang, D., Grüner, B.M., Kathiria, A.S., Ma, R.K., Vaka, D., Chu, P., Kozak, M., et al. (2017). BLIMP1 Induces Transient Metastatic Heterogeneity in Pancreatic Cancer. Cancer Discov. *7*, 1184–1199. https://doi.org/10.1158/2159-8290.CD-17-0250.

37. Corzo, C.A., Condamine, T., Lu, L., Cotter, M.J., Youn, J.-I., Cheng, P., Cho, H.-I., Celis, E., Quiceno, D.G., Padhya, T., et al. (2010). HIF-1α regulates function and differentiation of myeloid-derived suppressor cells in the tumor microenvironment. J. Exp. Med. *207*, 2439–2453. https://doi.org/10.1084/jem.20100587.

38. Feng, B., Bai, Z., Zhou, X., Zhao, Y., Xie, Y.-Q., Huang, X., Liu, Y., Enbar, T., Li, R., Wang, Y., et al. (2024). The type 2 cytokine Fc–IL-4 revitalizes exhausted CD8+ T cells against cancer. Nature *634*, 712–720. https://doi.org/10.1038/s41586-024-07962-4.

39. Novita Sari, I., Setiawan, T., Seock Kim, K., Toni Wijaya, Y., Won Cho, K., and Young Kwon, H. (2021). Metabolism and function of polyamines in cancer progression. Cancer Lett. *519*, 91–104. https://doi.org/10.1016/j.canlet.2021.06.020.

40. Bachmann, A.S., and Geerts, D. (2018). Polyamine synthesis as a target of MYC oncogenes. J. Biol. Chem. *293*, 18757–18769. https://doi.org/10.1074/jbc.TM118.003336.

41. Casero, R.A., Murray Stewart, T.M., and Pegg, A.E. (2018). Polyamine metabolism and cancer: treatments, challenges and opportunities. Nat. Rev. Cancer *18*, 681–695. https://doi.org/10.1038/s41568-018-0050-3.

42. Soda, K. (2011). The mechanisms by which polyamines accelerate tumor spread. J. Exp. Clin. Cancer Res. *30*, 95. https://doi.org/10.1186/1756-9966-30-95.

43. Mai, S., Liu, L., Jiang, J., Ren, P., Diao, D., Wang, H., and Cai, K. (2021). Oesophageal squamous cell carcinoma–associated IL-33 rewires macrophage polarization towards M2 via activating ornithine decarboxylase. Cell Prolif. *54*, e12960. https://doi.org/10.1111/cpr.12960.

44. Hayes, C.S., Shicora, A.C., Keough, M.P., Snook, A.E., Burns, M.R., and Gilmour, S.K. (2014). Polyamine-Blocking Therapy Reverses Immunosuppression in the Tumor Microenvironment. Cancer Immunol. Res. *2*, 274–285. https://doi.org/10.1158/2326-6066.CIR-13-0120-T.

45. Miska, J., Rashidi, A., Lee-Chang, C., Gao, P., Lopez-Rosas, A., Zhang, P., Burga, R., Castro, B., Xiao, T., Han, Y., et al. (2021). Polyamines drive myeloid cell survival by buffering intracellular pH to promote immunosuppression in glioblastoma. Sci. Adv. *7*, eabc8929. https://doi.org/10.1126/sciadv.abc8929.

46. Lawson, K., Larentowicz, L., Artim, S., Hayes, C.S., and Gilmour, S.K. (2006). A Novel Protein Kinase CK2 Substrate Indicates CK2 Is Not Directly Stimulated by Polyamines in Vivo. Biochemistry *45*, 1499–1510. https://doi.org/10.1021/bi052480i.

47. Yurekten, O., Payne, T., Tejera, N., Amaladoss, F.X., Martin, C., Williams, M., and O'Donovan, C. (2024). MetaboLights: open data repository for

metabolomics. Nucleic Acids Res. *52*, D640–D646. https://doi.org/10.1093/nar/gkad1045.

48. Tsugawa, H., Cajka, T., Kind, T., Ma, Y., Higgins, B., Ikeda, K., Kanazawa, M., VanderGheynst, J., Fiehn, O., and Arita, M. (2015). MS-DIAL: data-independent MS/MS deconvolution for comprehensive metabolome analysis. Nat. Methods *12*, 523–526. https://doi.org/10.1038/nmeth.3393.
49. Xia, J., Psychogios, N., Young, N., and Wishart, D.S. (2009). MetaboAnalyst: a web server for metabolomic data analysis and interpretation. Nucleic Acids Res. *37*, W652–W660. https://doi.org/10.1093/nar/gkp356.
50. Schneider, C.A., Rasband, W.S., and Eliceiri, K.W. (2012). NIH Image to ImageJ: 25 years of image analysis. Nat. Methods *9*, 671–675. https://doi.org/10.1038/nmeth.2089.
51. Suarez-Arnedo, A., Torres Figueroa, F.T., Clavijo, C., Arbeláez, P., Cruz, J. C., and Muñoz-Camargo, C. (2020). An image J plugin for the high throughput image analysis of in vitro scratch wound healing assays. PLoS One *15*, e0232565. https://doi.org/10.1371/journal.pone.0232565.
52. Heng, T.S.P., and Painter, M.W.; Immunological; Genome; Project Consortium (2008). The Immunological Genome Project: networks of gene expression in immune cells. Nat. Immunol. *9*, 1091–1094. https://doi.org/10.1038/ni1008-1091.
53. Blondel, V.D., Guillaume, J.-L., Lambiotte, R., and Lefebvre, E. (2008). Fast unfolding of communities in large networks. J. Stat. Mech. *2008*, 10008. https://doi.org/10.1088/1742-5468/2008/10/P10008.
54. Aibar, S., González-Blas, C.B., Moerman, T., Huynh-Thu, V.A., Imrichova, H., Hulselmans, G., Rambow, F., Marine, J.-C., Geurts, P., Aerts, J., et al. (2017). SCENIC: single-cell regulatory network inference and clustering. Nat. Methods *14*, 1083–1086. https://doi.org/10.1038/nmeth.4463.
55. Tang, Z., Kang, B., Li, C., Chen, T., and Zhang, Z. (2019). GEPIA2: an enhanced web server for large-scale expression profiling and interactive analysis. Nucleic Acids Res. *47*, W556–W560. https://doi.org/10.1093/nar/gkz430.
56. Li, T., Fu, J., Zeng, Z., Cohen, D., Li, J., Chen, Q., Li, B., and Liu, X.S. (2020). TIMER2.0 for analysis of tumor-infiltrating immune cells. Nucleic Acids Res. *48*, W509–W514. https://doi.org/10.1093/nar/gkaa407.
57. Newman, A.M., Liu, C.L., Green, M.R., Gentles, A.J., Feng, W., Xu, Y., Hoang, C.D., Diehn, M., and Alizadeh, A.A. (2015). Robust enumeration of cell subsets from tissue expression profiles. Nat. Methods *12*, 453–457. https://doi.org/10.1038/nmeth.3337.
58. Grosdidier, A., Zoete, V., and Michielin, O. (2011). SwissDock, a protein-small molecule docking web service based on EADock DSS. Nucleic Acids Res. *39*, W270–W277. https://doi.org/10.1093/nar/gkr366.
59. Zoete, V., Schuepbach, T., Bovigny, C., Chaskar, P., Daina, A., Röhrig, U. F., and Michielin, O. (2016). Attracting cavities for docking. Replacing the rough energy landscape of the protein by a smooth attracting landscape. J. Comput. Chem. *37*, 437–447. https://doi.org/10.1002/jcc.24249.
60. Wing, K., Onishi, Y., Prieto-Martin, P., Yamaguchi, T., Miyara, M., Fehervari, Z., Nomura, T., and Sakaguchi, S. (2008). CTLA-4 Control over Foxp3+ Regulatory T Cell Function. Science *322*, 271–275. https://doi.org/10.1126/science.1160062.
61. Buchou, T., Vernet, M., Blond, O., Jensen, H.H., Pointu, H., Olsen, B.B., Cochet, C., Issinger, O.-G., and Boldyreff, B. (2003). Disruption of the Regulatory β Subunit of Protein Kinase CK2 in Mice Leads to a Cell-Autonomous Defect and Early Embryonic Lethality. Mol. Cell. Biol. *23*, 908–915. https://doi.org/10.1128/MCB.23.3.908-915.2003.
62. Luche, H., Weber, O., Nageswara Rao, T., Blum, C., and Fehling, H.J. (2007). Faithful activation of an extra-bright red fluorescent protein in "knock-in" Cre-reporter mice ideally suited for lineage tracing studies. Eur. J. Immunol. *37*, 43–53. https://doi.org/10.1002/eji.200636745.
63. Mombaerts, P., Iacomini, J., Johnson, R.S., Herrup, K., Tonegawa, S., and Papaioannou, V.E. (1992). RAG-1-deficient mice have no mature B and T lymphocytes. Cell *68*, 869–877. https://doi.org/10.1016/0092-8674(92)90030-g.
64. Kranz, L.M., Diken, M., Haas, H., Kreiter, S., Loquai, C., Reuter, K.C., Meng, M., Fritz, D., Vascotto, F., Hefesha, H., et al. (2016). Systemic RNA delivery to dendritic cells exploits antiviral defence for cancer immunotherapy. Nature *534*, 396–401. https://doi.org/10.1038/nature18300.
65. Zeh, H.J., Perry-Lalley, D., Dudley, M.E., Rosenberg, S.A., and Yang, J.C. (1999). High avidity CTLs for two self-antigens demonstrate superior in vitro and in vivo antitumor efficacy. J. Immunol. *162*, 989–994. https://doi.org/10.4049/jimmunol.162.2.989.
66. Schmitt, F.C., ten Cate, V. ten, Fischer, Z., Hagen, M., Steigenberger, B.A., Tenzer, S., Wild, P.S., and Schmidlin, T. (2024). Metabolic Profiling of the EmDia Cohort by a Scalable DIA-LC-MS Workflow. https://doi.org/10.26434/chemrxiv-2024-53lds.
67. Wu, R., Chen, X., Kang, S., Wang, T., Gnanaprakasam, J.R., Yao, Y., Liu, L., Fan, G., Burns, M.R., and Wang, R. (2020). De novo synthesis and salvage pathway coordinately regulate polyamine homeostasis and determine T cell proliferation and function. Sci. Adv. *6*, eabc4275. https://doi.org/10.1126/sciadv.abc4275.
68. Alexander, E.T., Minton, A., Peters, M.C., Phanstiel, O., and Gilmour, S.K. (2017). A novel polyamine blockade therapy activates an anti-tumor immune response. Oncotarget *8*, 84140–84152. https://doi.org/10.18632/oncotarget.20493.
69. Ulges, A., Witsch, E.J., Pramanik, G., Klein, M., Birkner, K., Bühler, U., Wasser, B., Luessi, F., Stergiou, N., Dietzen, S., et al. (2016). Protein kinase CK2 governs the molecular decision between encephalitogenic TH17 cell and Treg cell development. Proc. Natl. Acad. Sci. USA *113*, 10145–10150. https://doi.org/10.1073/pnas.1523869113.
70. Muth, S., Schütze, K., Schild, H., and Probst, H.C. (2012). Release of dendritic cells from cognate CD4+ T-cell recognition results in impaired peripheral tolerance and fatal cytotoxic T-cell mediated autoimmunity. Proc. Natl. Acad. Sci. USA *109*, 9059–9064. https://doi.org/10.1073/pnas.1110620109.
71. Powrie, F., Leach, M.W., Mauze, S., Caddle, L.B., and Coffman, R.L. (1993). Phenotypically distinct subsets of CD4+ T cells induce or protect from chronic intestinal inflammation in C. B-17 scid mice. Int. Immunol. *5*, 1461–1471. https://doi.org/10.1093/intimm/5.11.1461.

STAR★METHODS

KEY RESOURCES TABLE

REAGENT or RESOURCE	SOURCE	IDENTIFIER
Antibodies		
Biotin anti-mouse Amphiregulin antibody	R&D Systems	RRID: AB_2060662
PerCP/Cy5.5 anti-mouse B220 antibody	BioLegend	RRID: AB_893354
BV711 anti-mouse CD103 antibody	BD Biosciences	RRID: AB_2738743
BUV496 anti-mouse CD103 antibody	BD Biosciences	RRID: AB_2870687
PE/Cy7 anti-mouse CD11b antibody	BioLegend	RRID: AB_312798
BV650 anti-mouse CD11b antibody	BioLegend	RRID: AB_11125575
APC-R700 anti-mouse CD11c antibody	BD Biosciences	RRID: AB_2744277
BV785 anti-mouse CD19 antibody	BioLegend	RRID: AB_11218994
PE/Cy5 anti-mouse CD19 antibody	BioLegend	RRID: AB_313645
FITC anti-mouse CD11c antibody	BioLegend	RRID: AB_313774
BV480 anti-mouse CD25 antibody	BD Biosciences	RRID: AB_2739522
PE/Cy5 anti-mouse CD3e antibody	BioLegend	RRID: AB_2894410
BB700 anti-mouse CD3e antibody	BD Biosciences	RRID: AB_2744393
BUV395 anti-mouse CD3e antibody	BD Biosciences	RRID: AB_2738278
BUV615 anti-mouse CD3e antibody	BD Biosciences	RRID: AB_2875439
BV510 anti-mouse CD4 antibody	BioLegend	RRID: AB_2564587
PE/Cy7 anti-mouse CD4 antibody	BioLegend	RRID: AB_312706
PE/Cy5 anti-mouse CD4 antibody	BioLegend	RRID: AB_312694
APC anti-mouse CD4 antibody	BioLegend	RRID: AB_312696
BV421 anti-mouse CD4 antibody	BioLegend	RRID: AB_10900241
BV786 anti-mouse CD4 antibody	BD Biosciences	RRID: AB_2738140
BUV496 anti-mouse CD4 antibody	BD Biosciences	RRID: AB_2813886
BUV737 anti-mouse CD4 antibody	BD Biosciences	RRID: AB_2870092
BV605 anti-mouse CD44 antibody	BioLegend	RRID: AB_2562451
BUV737 anti-mouse CD44 antibody	BD Biosciences	RRID: AB_2870126
APC-R700 anti-mouse CD44 antibody	BD Biosciences	RRID: AB_2739259
BV786 anti-mouse CD44 antibody	BD Biosciences	RRID: AB_2738395
BV421 anti-mouse CD45 antibody	BioLegend	RRID: AB_10899570
BV785 anti-mouse CD45 antibody	BioLegend	RRID: AB_2564590
PE-Dazzle 594 anti-mouse CD45 antibody	BioLegend	RRID: AB_2564002
BUV805 594 anti-mouse CD45 antibody	BD Biosciences	RRID: AB_2872789
PE-Dazzle 594 CD62L anti-mouse antibody	BioLegend	RRID: AB_2566162
BUV615 CD62L anti-mouse antibody	BD Biosciences	RRID: AB_2875828
PerCP/Cy5.5 anti-mouse CD64 antibody	BioLegend	RRID: AB_2561962
BV711 anti-mouse CD8a antibody	BioLegend	RRID: AB_2563510
BV650 anti-mouse CD8a antibody	BioLegend	RRID: AB_11124344
APC-R700 anti-mouse CD8a antibody	BD Biosciences	RRID: AB_2739032
BV510 anti-mouse CD8a antibody	BioLegend	RRID: AB_2563057
BUV563 anti-mouse CD8a antibody	BD Biosciences	RRID: AB_3675498
Alexa Fluor 647 anti-mouse F4/80 antibody	BioLegend	RRID: AB_893480
BV785 anti-mouse F4/80 antibody	BioLegend	RRID: AB_2563667
PerCP/Cy5.5 anti-mouse F4/80 antibody	BioLegend	RRID: AB_893484
FITC anti-mouse FOXP3 antibody	Thermo Fisher Scientific	RRID: AB_465243
PE-eFluor610 anti-mouse FOXP3 antibody	Thermo Fisher Scientific	RRID: AB_2574624

(*Continued on next page*)

Continued

REAGENT or RESOURCE	SOURCE	IDENTIFIER
PE/Cy7 anti-mouse FOXP3 antibody	Thermo Fisher Scientific	RRID: AB_891552
PerCP-eFluor 710 anti-mouse FOXP3 antibody	Thermo Fisher Scientific	RRID: AB_2811810
BV421 anti-mouse FOXP3 antibody	Thermo Fisher Scientific	RRID: AB_2925536
Alexa Fluor 488 anti-mouse GATA3 antibody	Thermo Fisher Scientific	RRID: AB_2574493
PE anti-mouse GATA3 antibody	Thermo Fisher Scientific	RRID: AB_1963600
eFluor 660 anti-mouse GATA3 antibody	Thermo Fisher Scientific	RRID: AB_10596663
FITC anti-mouse Ly6G/Ly6C (GR-1) antibody	BioLegend	RRID: AB_313371
BV421 anti-mouse Ly6G/Ly6C (GR-1) antibody	BioLegend	RRID: AB_10900232
APC anti-mouse Granzyme B antibody	Thermo Fisher Scientific	RRID: AB_2688068
PE anti-mouse Granzyme B antibody	Thermo Fisher Scientific	RRID: AB_10870787
FITC anti-mouse IFN-y antibody	BioLegend	RRID: AB_315399
BV605 anti-mouse IFN-y antibody	BioLegend	RRID: AB_2561438
eFluor 660 anti-mouse IL-13 antibody	Thermo Fisher Scientific	RRID: AB_2574279
PE anti-mouse IL-33R (ST2) antibody	BD Biosciences	RRID: AB_2744490
BV421 anti-mouse IL-33R (ST2) antibody	BD Biosciences	RRID: AB_2744489
PE-Dazzle 594 anti-mouse IL-4 antibody	BioLegend	RRID: AB_2564558
BV421 anti-mouse IL-4 antibody	BioLegend	RRID: AB_10896945
PE anti-mouse IL-5 antibody	BioLegend	RRID: AB_315328
PE anti-mouse ILT3 antibody	BioLegend	RRID: AB_2561653
Alexa Fluor 647 anti-mouse ILT3 antibody	BioLegend	RRID: AB_2562043
PE anti-mouse IRF4 antibody	BioLegend	RRID: AB_2563004
BV421 anti-mouse KLRG1 antibody	BioLegend	RRID: AB_2565613
PE-Dazzle 594 anti-mouse KLRG1 antibody	BioLegend	RRID: AB_2564050
BUV395 anti-mouse KLRG1 antibody	BD Biosciences	RRID: AB_2740018
PerCP-eFluor 710 anti-mouse LAG-3 antibody	Thermo Fisher Scientific	RRID: AB_11151334
BV510 anti-mouse I-A/I-E antibody	BioLegend	RRID: AB_2561397
BV650 anti-mouse I-A/I-E antibody	BioLegend	RRID: AB_2565975
PE/Cy5 anti-mouse NK-1.1 antibody	BioLegend	RRID: AB_493590
PE/Cy7 anti-mouse PD-1 (CD279) antibody	BioLegend	RRID: AB_572016
FITC anti-mouse PD-L2 (CD273/B7-DC) antibody	Thermo Fisher Scientific	RRID: AB_465462
PE anti-mouse SIGLEC-F antibody	BD Biosciences	RRID: AB_394341
FITC anti-mouse TCR b chain antibody	BioLegend	RRID: AB_313428
BV605 anti-mouse TCR b chain antibody	BioLegend	RRID: AB_2629563
PE anti-mouse TNF-a antibody	BioLegend	RRID: AB_315426
BV605 anti-mouse TNF-a antibody	BioLegend	RRID: AB_2563127
Anti-mouse Blimp-1 antibody	Thermo Fisher Scientific	RRID: AB_1907437
Anti-mouse CD31 antibody	Abcam	RRID: AB_2802125
Anti-mouse Siglec-F antibody	R&D Systems	RRID: AB_2286029
Rat IgG2A Isotype Control	R&D Systems	RRID: AB_357349
Ultra-LEAF™ Purified anti-mouse CD3ε Antibody	BioLegend	RRID: AB_2800555
Ultra-LEAF™ Purified anti-mouse CD28 Antibody	BioLegend	RRID: AB_11147170
IFN-γ Antibody, anti-mouse, pure-functional grade	Miltenyi Biotec	RRID: AB_10827685
IL-4 Antibody, anti-mouse, pure-functional grade	Miltenyi Biotec	RRID: AB_10828908
Chemicals, peptides, and recombinant proteins		
RPMI 1640	Thermo Fisher Scientific	Cat# 11875093
Fetal Bovine Serum	Gibco	Cat# 10437028
MEM Non-essential Amino Acid Solution (100×)	Sigma-Aldrich	Cat# M7145
DMEM	Thermo Fisher Scientific	Cat# 11500416
Eflornithine hydrochloride hydrate (DFMO)	MedChemExpress	Cat# HY-B0744B

(*Continued on next page*)

Continued

REAGENT or RESOURCE	SOURCE	IDENTIFIER
Oligofectamine	Thermo Fisher Scientific	Cat# 12252011
AMXT-1501 tetrahydrochloride	MedChemExpress	Cat# HY-124617A
DMAT	MedChemExpress	Cat# HY-15535
Ionomycin	Sigma-Aldrich	Cat# I9657
PMA	Sigma-Aldrich	Cat# P1585
eBioscience™ Monensin-solution (1000x)	Thermo Fisher Scientific	Cat# 00-4505-51
Recombinant Murine IL-2	Peprotech	Cat# 212-12
Spermidine trihydrochloride	Sigma-Aldrich	Cat# 85578-1G
M-PER™ Mammalian Protein Extraction Reagent	Thermo Fisher Scientific	Cat# 78501
Halt™ Phosphatase Inhibitor Single-Use Cocktail	Thermo Fisher Scientific	Cat# 78420
Halt™ Protease Inhibitor Cocktail, EDTA-Free (100X)	Thermo Fisher Scientific	Cat# 78437
Calcein AM, cell-permeant green and blue dyes	Thermo Fisher Scientific	Cat# C1430
BD Pharmingen™ DRAQ7™	BD Biosciences	Cat# 564904
Recombinant Murine IL-4	Peprotech	Cat# 214-14
Dako EnVision™ Flex Target Retrieval Solution low pH	Agilent	Cat# K800521-2
Dako EnVision™ Flex HRP Magenta Chromogen	Agilent	Cat# GV90011-2
Mouse IL-4, premium grade	Miltenyi Biotec	Cat# 130-097-761
Mouse IL-2 IS, premium grade	Miltenyi Biotec	Cat# 130-120-331
Mouse IL-12	Miltenyi Biotec	Cat# 130-096-707
Fixable Viability Dye eFluor 780	Thermo Fisher Scientific	Cat# 65-0865-18
DNA ScreenTape Analysis D1000 - Reagents	Agilent	Cat# 5067-5583
DNA ScreenTape Analysis D1000 – Sample Buffer	Agilent	Cat# 5067-5602
High Sensivity RNA ScreenTape Analysis – Sample Buffer	Agilent	Cat# 5067-5580
Critical commercial assays		
AbsoluteIDQ® p180 kit	Biocrates	Cat# 20073.6
Total Polyamine Assay Kit	Abcam	Cat# ab239728
Tumor Dissociation Kit, mouse	Miltenyi Biotec	Cat# 130-096-730
CD45 (TIL) MicroBeads, mouse	Miltenyi Biotec	Cat# 130-110-618
CD4/CD8 (TIL) MicroBeads, mouse	Miltenyi Biotec	Cat# 130-116-480
CD4 (TIL) MicroBeads, mouse	Miltenyi Biotec	Cat# 130-116-475
eBioscience™ Foxp3/Transcription Factor Staining Buffer Set	Thermo Fisher Scientific	Cat# 00-5523-00
CD4+CD25+ Regulatory T Cell Isolation Kit, mouse	Miltenyi Biotec	Cat# 130-091-041
CD8a+ T Cell Isolation Kit, mouse	Miltenyi Biotec	Cat# 130-104-075
Naive CD4+ T Cell Isolation Kit, mouse	Miltenyi Biotec	Cat# 130-104-453
CD11c MicroBeads UltraPure, mouse	Miltenyi Biotec	Cat# 130-125-835
Rat-on-Mouse HRP-Polymer	Biocare	Cat# RT517
Mouse on Mouse Polymer IHC Kit	Abcam	Cat# ab269452
Dynabeads™ Mouse T-Activator CD3/CD28 for T-Cell Expansion and Activation	Thermo Fisher Scientific	Cat# 11453D
Mouse Amphiregulin DuoSet ELISA	R&D Systems	Cat# DY989
Mouse VEGF DuoSet ELISA	R&D Systems	Cat# DY493
Mouse IL-10 DuoSet ELISA	R&D Systems	Cat# DY417
Mouse TGF-beta 1 DuoSet ELISA	R&D Systems	Cat# DY1679
Mouse IFN-gamma DuoSet ELISA	R&D Systems	Cat# DY485
CycLex® CK2(Casein kinase II) Kinase Assay/Inhibitor Screening Kit	MBL Life Science	Cat# CY-1170
Pierce™ Bradford Protein Assay Kit	Thermo Fisher Scientific	Cat# 23200
RNeasy Micro Kit	Qiagen	Cat# 74004

(*Continued on next page*)

Continued

REAGENT or RESOURCE	SOURCE	IDENTIFIER
Agilent RNA 6000 Pico Kit	Agilent	Cat# 5067-1513
SMART-Seq v4 Ultra Low Input RNA Kit for Sequencing	Takara Bio	Cat# 634888
SMARTer® Stranded Total RNA-Seq Kit v2 - Pico Input Mammalian	Takara Bio	Cat# 634411
Nextera XT DNA Library Preparation Kit	Illumina	Cat# FC-131-1024
HiSeq Rapid SR SBS Kit v2	Illumina	Cat# FC-402-4021
BD™ Ms Single Cell Sample Multiplexing Kit	BD Biosciences	Cat# 633793
BD Rhapsody™ Enhanced Cartridge Reagent Kit	BD Biosciences	Cat# 664887
BD Rhapsody™ Cartridge Kit	BD Biosciences	Cat# 633733
BD Rhapsody™ cDNA Kit	BD Biosciences	Cat# 633773
BD Rhapsody™ Whole Transcriptome Analysis (WTA) Amplification Kit	BD Biosciences	Cat# 633801
Visium FFPE Reagent Kit v2 - Small PN-1000436	10X Genomics	Cat# PN-1000436
Visium Mouse Transcriptome Probe Set v1.0	10X Genomics	Cat# PN-1000365
Visium CytAssist Reagent Accessory Kit	10X Genomics	Cat# PN-1000499
Visium CytAssist Spatial Gene Expression for FFPE, Mouse Transcriptome, 6.5 mm, 4 rxns*	10X Genomics	Cat# PN-1000521
qScriber™ cDNA Synthesis Kit	highQu	Cat# RTK0101
CellTrace™ Violet Cell Proliferation Kit, for flow cytometry	Thermo Fisher Scientific	Cat# C34557
Hot Start Taq EvaGreen qPCR Mix	Axon Labortechnik	Cat# 27488
Qubit™ 1X dsDNA HS Assay Kit	Thermo Fisher Scientific	Cat# Q33230
Qubit™ RNA High Sensitivity (HS) Assay Kit	Thermo Fisher Scientific	Cat# Q32855
Deposited data		
Murine mRNASeq data	This paper	GEO: GSE296432
Murine mRNASeq data	This paper	GEO: GSE237146
Murine mRNASeq data	This paper	GEO: GSE237147
Murine scRNASeq data	This paper	GEO: GSE296534
Murine Spatial Transcriptomics data	This paper	GEO: GSE296660
Metabolomics data	This paper	MTBLS: MTBLS12633
Murine mRNASeq data	Delacher et al.[35]	ENA: PRJEB14591
Experimental models: Cell lines		
B16.F10 OVA	provided by M.Diken	CVCL_0159
MC38	provided by H-C. Probst	CVCL_B288
NIH 3T3	N/A	CVCL_0594
Experimental models: Organisms/strains		
C57BL/6J	Charles River Lab	https://www.criver.com/
Csnk2b$^{fl/fl}$ (*Csnk2b*$^{tm1.2Bb}$)	provided by Boldyreff Lab	N/A
Foxp3-IRES-Cre (*Foxp3*$^{tm1(cre)Saka}$)	provided by Sakagushi Lab	N/A
Rosa26-RFP (*Gt(ROSA)26Sor*^{tm1Hjf})	provided by Waismann Lab	N/A
Csnk2b$^{Treg-/-}$ (*Csnk2b*$^{tm1.2Bb}$ *Foxp3*$^{tm1(cre)Saka}$)	Bopp Lab	N/A
Rosa26-RFP x Csnk2b$^{Treg-/-}$ (*Gt(ROSA)26Sor*^{tm1Hjf} *Csnk2b*$^{tm1.2Bb}$ *Foxp3*$^{tm1(cre)Saka}$)	Bopp Lab	N/A
CD90.1^{+} mice (B6.PL-*Thy1*$^{a/CyJ}$)	provided by Waismann Lab	N/A
Ly5.1^{+} mice (B6.SJL-Ptprc^{a}*Pepc*$^{b/BoyCrl}$)	provided by Probst Lab	N/A
Foxp3-Cre x *PParg*$^{fl/fl}$ mice (B6.129(Cg)-*Foxp3*$^{tm4(YFP/icre)Ayr}$/J *Pparg*^{tm1Gonz})	provided by Beyer Lab	N/A
RAG1 KO mice (B6.129S7-*Rag1*$^{tm1Mom/J}$)	Charles River Lab	https://www.criver.com/
Oligonucleotides		
Odc1 siRNA	Santa Cruz Biotechnology	Cat# sc-44573
control siRNA-E	Santa Cruz Biotechnology	Cat# sc-44233

(*Continued on next page*)

Continued

REAGENT or RESOURCE	SOURCE	IDENTIFIER
Hprt, 5′-GTTGGATACAGGCCAGACTTTGT-3′ (forward)	Sigma	N/A
Hprt, 5′-GAGGGTAGGCTGGCCTATAGGCT-3′ (reverse)	Sigma	N/A
Lilrb4a, 5'- ATGGGCACAAAA AGAAGGCTAA (forward)	Sigma	N/A
Lilrb4a, 5'- GGCA TAGGTTACATCCTGGGTC-3' (reverse)	Sigma	N/A
Odc1, 5′-GACGAGTTTGACTGCCACATC-3′ (forward)	Sigma	N/A
Odc1, 5′-CGCAACATAGAACGCATCCTT-3′ (reverse)	Sigma	N/A
Software and algorithms		
MS-DIAL (5.4.241021)	Arita et al.[48]	https://github.com/systemsomicslab/MsdialWorkbench
MetaboAnalyst (6.0)	Wishart et al.[49]	https://www.metaboanalyst.ca/home.xhtml
ImageJ (1.54g)	Eliceiri et al.[50]	https://imagej.net/ij/index.html
Wound Healing size tool (plugin for ImageJ	Muñoz-Camargo et al.[51]	https://github.com/AlejandraArnedo/Wound-healing-size-tool/wiki#wound-healing-size-tool
Evolve	PamGene International	N/A
CLC Genomics Work Bench (24.0.2)	Qiagen	N/A
Partek Flow software (10.0)	Illumina	N/A
Immunological Genome Project	Immunological Genome Project Consortium et al.[52]	https://rstats.immgen.org/MyGeneSet_New/index.html
Louvain algorithm	Lefebvre et al.[53]	N/A
AUCell algorithm	Aerts et al.[54]	N/A
Space Ranger (2.1.0)	10X Genomics	N/A
GEPIA2	Zhang et al.[55]	http://gepia2.cancer-pku.cn/#index
TIMER 2.0	Liu et al.[56]	https://cistrome.shinyapps.io/timer/
CIBERSORT algorithm	Alizadeh et al.[57]	N/A
SwissDock	Michielin et al.[58]	https://www.swissdock.ch/
Attracting Cavities algorithm	Michielin et al.[59]	N/A
FlowJo v10.0.7	FlowJo, LLC	https://flowjo.com/
Prism 10 v10.3.0	GraphPad	https://www.graphpad.com/
FACS Diva (v8.0.2)	BD Biosciences	https://www.bdbiosciences.com/en-us/products/software/instrument-software/bd-facsdiva-software
SpaceRanger v2.1.0	10x Genomics	https://www.10xgenomics.com/products/visium-analysis
Chimera (1.18)	Ferrin et al.[27]	https://www.cgl.ucsf.edu/chimera/download.html
Other		
Amicon® Ultra Centrifugal Filter, 10 kDa MWCO	Merck	Cat# UFC501096
Kinetex 2.6 μm F5 100 Å, LC Column 150 x 2.1 mm	Phenomenex	Cat# 00F-4723-AN
gentleMACS™ C Tubes	Miltenyi Biotec	Cat# 130-093-237
Culture-Insert 2 Well in μ-Dish 35 mm	Ibidi	Cat# 81176
Hair removal creme	Veet	N/A
PTK-196 PamChip	PamGene International	Cat# 81176
Epredia™ SuperFrost Plus™ Adhäsionsobjektträger	Thermo Fisher Scientific	Cat# 10149870
AMPure XP Reagent	Beckmann Coulter	Cat# A63881
PE Streptavidin	BioLegend	Cat# 405204
DNA ScreenTape Analysis D1000 - Screen Tape	Agilent	Cat# 5067-5586
DNA ScreenTape Analysis D1000 - Ladder	Agilent	Cat# 5067-5586
High Sensivity RNA ScreenTape Analysis – Screen Tape	Agilent	Cat# 5067- 5579
High Sensivity RNA ScreenTape Analysis – Ladder	Agilent	Cat# 5067- 5581

EXPERIMENTAL MODEL AND STUDY PARTICIPANT DETAILS

Mice

C57BL/6J mice were obtained from Charles River Laboratories. BALB/c Foxp3-IRES-Cre mice (*Foxp3* $^{tm1(cre)Saka}$) were provided by S. Sakaguchi and backcrossed at least 12 times to obtain C57BL/6J Foxp3-IRES-Cre mice.[60] Mice carrying a *loxP*-flanked *Csnk2b* allele (*Csnk2b*$^{fl/fl}$) on the C57BL/6J background (*Csnk2b*$^{tm1.2Bb}$) were provided by B. Boldyreff.[61] To obtain *Csnk2b*$^{fl/fl}$ *Foxp3*-Cre mice (*Csnk2b*$^{Treg-/-}$; *Csnk2b*$^{tm1.2Bb}$ *Foxp3*$^{tm1(cre)Saka}$), *Csnk2b*$^{fl/fl}$ mice and C57BL/6J *Foxp3*-IRES-Cre mice were intercrossed. In all experiments, *Csnk2b*$^{fl/fl}$ littermates served as controls. *Rosa26*-RFP (red fluorescent protein) reporter mice (*Gt(Rosa)26Sor*^{tm1Hjf}/J) and CD90.1^{+} C57BL/6J (B6.PL-*Thy1*$^{a/CyJ}$) mice were kindly provided by Ari Waismann.[62] *Rosa26*-RFP *Csnk2b*$^{fl/fl}$ *Foxp3*-Cre mice were obtained by intercrossing these lines accordingly. Ly5.1^{+} C57BL/6J (B6.SJL-Ptprc^{a}*Pepc*$^{b/BoyCrl}$) mice were kindly provided by H.C. Probst. Mice with a T_{reg} cell-specific (deletion of the peroxisome proliferator-activated receptor gamma (*PPARγ*$^{-/-}$, B6.129(Cg)-*Foxp3*$^{tm4(YFP/icre)Ayr}$/J *Pparg*^{tm1Gonz}) were kindly provided by Marc Beyer.[33] C57BL/6J mice deficient in recombination-activating gene 1 (B6.129S7-*Rag1*$^{tm1Mom/J}$) were obtained from Charles River Laboratories.[63] Animals were used at 8 to 20 weeks of age. All animals were housed under specific pathogen-free (SPF) conditions using institutionally approved protocols (permission was e.g. obtained from the Landesuntersuchungsamt Koblenz). Animal experiments were conducted under the supervision of authorized investigators and in accordance with European Union guidelines and relevant ethical regulations. A maximum of five mice were housed per cage, and only littermates were grouped together to minimize variability. Standard chow and water were provided *ad libitum*. Enrichment (e.g., nesting material and shelter) was provided in all cages. Health status was regularly monitored, and cages were changed once per week. Littermate animals were used for group allocation when available. Both sexes were included in all experiments; no animals were excluded based on sex. Whenever feasible, equal numbers of male and female mice were distributed across experimental groups. Based on our observations, sex did not influence the experimental outcomes. For *in vivo* studies with larger cohorts, animals were grouped irrespective of sex and matched by age as closely as possible, preferably using littermates or, if not feasible, age-matched animals within a ± 4-week range.

Cell lines and cell culture

OVA-expressing B16.F10 melanoma cells (derived from male C57BL/6 mice) were kindly provided by M. Diken (Translationale Onkologie, University Medical Center, Johannes Gutenberg University Mainz).[64] B16.F10 cells were cultured for 1 week (37°C; 5% CO_2, Humidity: 95 ± 5%) before inoculation in RPMI 1640 (Thermo Fisher Scientific, #11875093) supplemented with 1% penicillin–streptomycin, 10% FCS (Gibco; # 10437028), 2 mM glutamine, 1% NEAA (Sigma, #M7145) and 50 μM β-mercaptoethanol. MC38 colon adenocarcinoma cells were kindly provided by Hans-Christian Probst (Institute for Immunology University Medical Center, Johannes Gutenberg University Mainz).[65] Before inoculation MC38 cells (derived from female C57BL/6 mice) were cultured for 1 week in DMEM (Thermo Fisher Scientific; 11500416) supplemented with 1% penicillin–streptomycin, 10% FCS, 2 mM glutamine and 1 mM sodium pyruvate. The cell cultures were routinely monitored to ensure confluency remained below 80%. NIH 3T3 cells were routinely cultured in DMEM supplemented with 2% FCS, 2 mM glutamine, 1 mM sodium pyruvate, and 1% penicillin/streptomycin to maintain a confluence level of no more than 80%. All cell lines were regularly tested for mycoplasma contamination. All cell lines were maintained at 37 °C in a humidified incubator with 5% CO_2. Research Resource Identifiers (RRIDs) for the cell lines used in this study are listed in the key resources table.

METHOD DETAILS

Biogenic amines profiling by mass spectrometry

For tumor metabolite extraction, 2×10^5 B16.F10 cells or 1×10^6 MC38 cells were subcutaneously (s.c.) injected into the right flank of C57BL/6J mice. Tumors were harvested at a volume of ~200 mm^3, rinsed with 1 ml ethanol/PBS (85:15), and the extract was collected and centrifuged. For skin metabolite extraction, equal amounts of shaved and depilated flank skin were homogenized in 1 ml ethanol/PBS (85:15), followed by centrifugation. In both cases, 10 μl of the supernatant was used for analysis. Targeted metabolomics were performed using the AbsoluteIDQ® p180 kit (Biocrates; 20073.6) and UPLC®-MS/MS (Waters). Samples were analyzed in technical duplicates using MetaboINDICATOR software (Biocrates).

Total Polyamine Assay

Polyamine concentrations were quantified in sera from healthy and tumor-bearing mice, B16.F10 cell lysates (transfected with non-targeting or *Odc1* siRNA), and wild-type versus CK2β-deficient T_{reg} cell lysates using the Total Polyamine Assay Kit (Abcam, ab239728). Cell lysates were prepared from 1×10^6 cells by repeated freeze-thaw cycles in assay buffer. Sera and lysates were incubated with clean-up mix (1:50) for 30 min at room temperature, then filtered through 10 kDa cut-off columns (Merck, UFC501096) by centrifugation at 10,000 × g for 20 min at 4°C. 50 μl of filtrates were used for polyamine quantification according to manufacturer's instructions.

B16.F10 cell metabolome analysis

B16.F10 cells were cultured in the presence or absence of 1 mM DFMO (HY-B0744B; MedChemExpress) for 48 hours. Processing of the samples and measurement were performed as previously described.[66] Briefly, metabolite extracts of 1×10^6 B16.F10 cells were

prepared by adding 300 µl of -20°C cold lysis buffer (80% methanol / 20% water) for protein-precipitation followed by centrifugation at 24.400 × g for 30 min. Supernatant was transferred to a new tube and evaporated under constant nitrogen flow. Dried metabolites were resuspended in 10 µL water. The equivalent of 100.000-200.000 cells were analyzed by liquid chromatography - mass spectrometry (LC-MS) using an Agilent 1290 Infinity II coupled to a SCIEX ZenoTOF 7600. Metabolites were separated on a Phenomenex Kinetex F5 2.6 µm (2.1mm x 150 mm) column using a linear gradient from 0.1% formic acid (FA) in water to 0.1% FA in 95% acetonitrile (ACN) / 5% water. MS spectra were acquired in positive ion mode using a precursor ion mass range of 70 – 1000 m/z. Per cycle top 11 precursor ions were subjected to fragmentation using data-dependent acquisition. MS/MS spectra were recorded in the mass range of 40–1000 m/z, with Zeno pulsing enabled. LC-MS data was processed in MS-DIAL (ver. 5.4.241021)[48] using untargeted spectral matching against the public ESI(+)-MS/MS library from authentic standards and an in-house spectral library. Reference matched metabolites were used for further analysis. The raw data were analyzed employing MetaboAnalyst 6.0 (https://www.metaboanalyst.ca/).[49]

Subcutaneous tumor mouse models

B16.F10 cells (2×10^5 in 100 µL PBS) or MC38 cells (1×10^6 in 100 µL PBS) were s.c. injected into the right flank of 10-16-week-old syngeneic male and female C57BL/6J, *Csnk2b*$^{fl/fl}$ and *Csnk2b*$^{Treg-/-}$ mice. Tumor growth was assessed 7 days post-injection over a period of 7–14 days. Tumor size was measured using a caliper and tumor volume was calculated using the formula: (width^2 × length) × 0.5 Mice were euthanized upon tumor necrosis or when tumors exceeded 2 cm in any direction. For *in vitro* polyamine depletion, B16.F10 cells were pre-treated with 1 mM DFMO (MedChemExpress; HY-B0744B) for 48 hours or transfected with 50 nM *Odc1* siRNA (Santa Cruz, sc-44573) for 48 hours using Oligofectamine (Thermo Fisher; 12252011) according to manufacturer's instructions. Scrambled siRNA (Santa Cruz Biotechnology; sc-44233) served as control. *Odc1* knockdown efficiency was verified by qPCR. To assess the therapeutic effect of polyamine depletion *in vivo*, tumor-bearing *Csnk2b*$^{fl/fl}$ and *Csnk2b*$^{Treg-/-}$ mice received DFMO (1% w/v) in drinking water (*ad libitum*) and intraperitoneal (i.p.) AMXT-1501 (HY-124617; MedChemExpress) (3 mg/kg body weight in PBS) administered every 48 hours post-inoculation. Dosing was based on previous studies.[44,67,68] For eosinophil depletion, α-SIGLEC-F antibody (R&D Systems; 238047) (15 µg in 50 µl PBS) was administered i.p. on days 7, 10, 14, and 17 post-inoculation; control mice received isotype-matched rat IgG2A (R&D Systems; MAB006). CK2 inhibition was performed using DMAT (MedChemExpress; HY-15535) (10 mg/kg body weight in DMSO/ethanol), injected s.c. on days 9, 11, 14, 17, and 20.[69]

Tumor dissociation for single-cell suspension

Mice were euthanized by CO_2 inhalation and tumors were carefully excised from the surrounding skin. Tumors were cut into 2-4 mm pieces, transferred to gentleMACS™ C Tubes (Miltenyi Biotec, 130-093-237), and digested using the Mouse Tumor Dissociation Kit (Miltenyi Biotec, 130-096-730) with the gentleMACS™ Octo Dissociator with Heaters (Miltenyi Biotec; 130-096-427) according to the manufacturer's instructions. Cell suspensions were sequentially filtered through 70 µm and 40 µm cell strainers and resuspended in FACS buffer (PBS + 0.5% BSA + 0.01% sodium azide + 2 mM EDTA) for flow cytometry or cell sorting.

Isolation of tumor-infiltrating lymphocytes

CD45$^+$, CD8$^+$ and/or CD4$^+$ tumor-infiltrating lymphocytes were isolated using CD45 (TILs) (Miltenyi Biotec; 130-110-618), CD4/CD8 (TILs) (Miltenyi Biotec; 130-116-480) or CD4 (TILs) (Miltenyi Biotec; 130-116-475) Microbeads according to the manufacturer's instructions by magnetic activated cell sorting (MACS).

Flow cytometric analysis

Flow cytometry was performed on FACSymphony A5 or LSR II cytometers (BD Biosciences), and data were analyzed using FlowJo v10 (BD). For surface staining, cells were incubated with antibodies against indicated markers and fixable viability dye 780 (Thermo Fisher; 65-0865-14) for 30 min at 4 °C. Intracellular staining was conducted using the Foxp3/Transcription Factor Staining Buffer Set (Thermo Fisher; 00-5523-00) following the manufacturer's instructions. Cytokine production was assessed after 4 h stimulation with 20 ng/mL PMA (Sigma–Aldrich; P1585), 1µM ionomycin (Sigma–Aldrich; I9657), and monensin (Thermo Fisher; 00-4505-51).

Magnetic Cell Isolation (MACS)

Spleens and lymph nodes from C57BL/6J, *Csnk2b*$^{fl/fl}$ or *Csnk2b*$^{Treg-/-}$ mice were mechanically disrupted and passed through 40 µm cell strainers. Erythrocytes were lysed using Gey's buffer, followed by additional filtration (40 µm cell strainers). Live cells were counted microscopically using trypan blue exclusion. CD4$^+$CD25$^+$ T cells (T_{reg} cells) (Miltenyi Biotec; 130-091-041), CD8$^+$ T cells (Miltenyi Biotec; 130-104-075), naive CD4$^+$CD62L$^+$CD44$^-$ T cells (Miltenyi Biotec; 130-104-453), and CD11c$^+$ cells (Miltenyi Biotec; 130-125-835) were isolated using magnetic bead-based kits according to the manufacturer's instructions. Post-sort purities ranged from 85–95% for T_{reg} cells and CD11c$^+$ cells, and > 90% for CD8$^+$ and naive CD4$^+$ T cells.

Culture of *ex vivo* CD4$^+$ CD25$^+$ cells

MACS-purified CD4$^+$CD25$^+$ T cells (2×10^5 per well) were stimulated in Iscove's Modified Dulbecco's Medium (Sigma) supplemented with 10% FCS, 2 mM L-glutamine, 1 mM sodium pyruvate, and 1% penicillin/streptomycin. Cells were cultured in 96-well flat-bottom plates at 37 °C and 5% CO_2 for 48 hours for flow cytometry and CK2 kinase activity assay or 72 hours for mRNA-seq, supernatants for wound healing assay and supernatants for IL-10 respectively TGF-β1 ELISA. Stimulation included 200ng/ml recombinant murine IL-2

(Peprotech; 212-12), α-CD3/CD28 Expander Beads (Thermo Fisher; 11452D) (3:1 bead-to-cell ratio), and either DFMO (1 mM) and/or spermidine (2.5 μM; Sigma; 85578-1G). For AREG ELISA, cells were washed after 72 hours, counted, and 2×10^5 live cells were re-cultured for 24 hours without DFMO or spermidine.

Enzyme-linked immunosorbent assay (ELISA)

AREG, VEGF, IL-10, and TGF-β1 concentrations in $CD4^+CD25^+$ T cell culture supernatants were measured using DuoSet ELISA kits from R&D Systems (DY989, DY493, DY417, DY1679) according to the manufacturer's instructions. IFN-γ levels in co-culture supernatants ($CD8^+$ T cells or T_H1 cells + T_{reg} cells) were quantified using the Mouse IFN-γ DuoSet ELISA kit (R&D Systems; DY485).

Wound healing assay

For the *in vitro* wound healing assay, 2×10^4 3T3 cells were seeded into each chamber of a 2-well culture insert (Ibidi; #81176) in DMEM + 2% FCS and cultured for 24 hours to form a monolayer. After removal of the insert (500 μm cell-free gap), wells were washed with PBS and overlaid with 300 μL DMEM plus 100 μL $CD4^+CD25^+$ T cell culture supernatant. Cells were incubated for 16 hours. Images were acquired before and after incubation using a Rebel Hybrid microscope (Echo), and gap closure was quantified using ImageJ software with the Wound Healing Size Tool.[50,51] Gap closure (%) was calculated as: [(gap size at 0 h – gap size at 16 h) / gap size at 0 h] × 100.

CK2 kinase activity assay

Cultured $CD4^+CD25^+$ T cells were counted using trypan blue exclusion, and 1×10^6 cells were lysed in 50 μL M-PER™ buffer (Thermo Fisher; 78501) supplemented with HALT™ phosphatase (Thermo Fisher; 78420) and protease (Thermo Fisher; 78437) inhibitors. After 15 min lysis on ice and centrifugation, 10 μL of the supernatant were used to assess CK2 activity using the CycLex CK2 Assay Kit (MBL Life Science; CY-1170) per the manufacturer's protocol. CK2 activity was normalized to total protein content measured with the Pierce™ Coomassie Plus (Bradford) Assay Kit (Thermo Fisher; 23200).

Kinase activity profiling

To analyze the tyrosine kinase (PTK) activity in splenic *ex vivo* isolated $CD4^+$ $CD25^+$ cells from *Csnk2b*$^{fl/fl}$ and *Csnk2b*$^{Treg-/-}$ mice, the PamStation®12 in combination with the PTK® PamChip (PamGene International) was utilized according to the manufacturer's protocol. Lysis of MACS-enriched $CD4^+CD25^+$ T cells and determination of the total protein concentration in the lysates were carried out as described in the previous section. The PTK PamChips contain 196 consensus phosphopeptide sequences per well, immobilized on porous ceramic membranes. PTK PamChips® were pre-treated with 2% bovine serum albumin (BSA) to block non-specific binding sites. Subsequently, cell lysates (protein concentration 0.2 μg/μL) were added to each PTK PamChip®. Following this, a kinase reaction mixture comprising kinase buffer, dithiothreitol (DTT), kinase additives, BSA, fluorescent antibodies, and a final concentration of 400 μM ATP was added to each PTK PamChip®. The homogenized samples containing active kinases and assay mixtures were pumped through the wells to allow interaction between kinases in the sample and specific peptide substrates immobilized on the chip. Real-time measurement of phosphorylation levels per well was conducted using Evolve (PamGene) kinetic image capture software. This software records the binding of FITC-labeled α-phospho antibodies to each phosphorylated peptide substrate at 6-second intervals over a duration of 60 minutes. Quality control and data processing were performed by PamGene using their standardized pipeline.

mRNA sequencing

mRNA sequencing was conducted on untreated and DFMO-treated α-CD3/28-stimulated $CD4^+CD25^+$ cells from *Csnk2b*$^{fl/fl}$ and *Csnk2b*$^{Treg-/-}$ mice, *ex vivo*-sorted conventional $CD4^+FOXP3^-$ T cells ($CD4^+$ T_{conv} cells) from tumors of *Csnk2b*$^{fl/fl}$ and *Csnk2b*$^{Treg-/-}$ mice using Rosa26-RFP reporter mice, and *ex vivo*-sorted $ILT3^-$ and $ILT3^+CD4^+CD25^+$ cells from C57B/6J mice. Tumor-infiltrating $CD4^+$ T_{conv} ($TCR\beta^+CD4^+RFP^-$) cells were sorted using a FACSAria III (BD Biosciences) from Rosa26-RFP *Csnk2b*$^{Treg-/-}$ mice and Rosa26-RFP *Csnk2b*$^{fl/fl}$ littermates. $ILT3^-$ and $ILT3^+CD4^+CD25^+$ cells from the spleen and mesenteric lymph nodes of C57BL/6J mice were sorted using a FACSAria II (BD Biosciences). RNA preparation was conducted using the RNeasy Micro Kit (Qiagen; 74004). RNA quantity was determined with a Qubit 2.0 fluorometer (Invitrogen), and RNA quality was assessed on a Bioanalyzer 2100 (Agilent) using the RNA 6000 Pico Chip Kit (Agilent; 5067-1513) to determine the RNA integrity number (RIN value). Samples with a RIN >8 were used for library preparation. cDNA synthesis for *ex vivo*-isolated $CD4^+$ $CD25^+$ cells, tumor-infiltrating $CD4^+$ T_{conv} cells was performed with the SMART-Seq v4 Ultra Low Input RNA Kit for Sequencing (Takara Bio; 634888) using a total RNA input of 100 ng ($CD4^+$ $CD25^+$ cells) and 2 ng (tumor-infiltrating $CD4^+$ T_{conv} cells). cDNA synthesis for $ILT3^-$/$ILT3^+$ $CD4^+CD25^+$ cells was conducted with the SMARTer Kit V2 (Takara Bio; 634411) using a total input of 1 ng of total RNA. The Nextera XT DNA Library Preparation Kit (Illumina; FC-131-1024) was used for library preparation. Sequencing of *ex vivo* $CD4^+$ $CD25^+$ cells was performed on a NovaSeq 6000 (Novogene) using a HiSeq Rapid SR SBS Kit v2 (150 cycles) for cluster generation, with an average of 30×10^6 reads per sample. Sequencing of tumor-infiltrating $CD4^+$ T_{conv} cells was conducted on a HiSeq2500 (Illumina) using a HiSeq Rapid SR SBS Kit v2 (150 cycles) for cluster generation, with an average of 15×10^6 reads per sample. Sequencing of $ILT3^+$/$ILT3^-CD4^+CD25^+$ cells was performed on a MiSeq instrument (Illumina) with a HiSeq Rapid SR SBS Kit v2 (150 cycles) for cluster generation, with an average of 12-15$\times10^6$ reads per sample. Sequencing data were analyzed using the CLC Genomics Work Bench (Qiagen).

Single cell mRNA Sequencing

2×10^5 B16.F10 cells were inoculated in *Csnk2b*$^{fl/fl}$ and *Csnk2b*$^{Treg-/-}$ mice and CD4$^+$ and CD8$^+$ TILs were isolated as described in the previous section. Single cell capturing, RNA isolation and cDNA synthesis were performed using the BD Rhapsody Single-Cell Analysis System (BD Biosciences) according to manufacturer's instructions (Workflow and reagents are described in detail in the BD Biosciences document Doc ID: 210966 Rev1.0 and are also listed in the Key Resources Table). Each sample was tagged with a unique sample barcode for multiplexing on the same cartridge. Whole transcriptome libraries and sample tag libraries were created using BD WTA Amplification Kit (BD Biosciences,633801) with random primers followed by amplification and insertion of sequencing adaptors following the BD Rhapsody System mRNA WTA and Sample Tag Library Preparation Protocol (BD Biosciences, Doc ID: 23-24119 Rev1.0). Library quality and concentration were assessed using the Bioanalyzer2100 (Agilent). Sequencing (paired end reads, PE150) was performed on a NovaSeq 6000 (Illumina) at Novogene (Cambridge; UK). Transcript alignment, quantification, and demultiplexing were performed using the BD Rhapsody WTA analysis pipeline following Illumina standard preprocessing protocols. Output files ("RSEC Mols per Cell") were imported into Partek Flow software (v10.0) for downstream analysis. Cells were filtered based on quality control thresholds, excluding those with fewer than 500 or more than 4000 detected genes, or with mitochondrial gene content exceeding 10%. Low-expression genes were removed if detected in less than 1% of all cells. Contaminating non-T cell populations were excluded by comparing gene expression profiles to reference immune cell signatures provided by the ImmGen Consortium (https://www.immgen.org/).[52] Normalization and downstream analysis were performed using Partek Flow's default pipeline. Raw single-cell counts were normalized by counts per million (CPM), followed by $\log_2$ transformation (Add:1). Principal component analysis (PCA) was used for dimensionality reduction, and cells were clustered using the Louvain algorithm[53] with standard settings. Uniform Manifold Approximation and Projection (UMAP) was applied for two-dimensional visualization. Cell populations were annotated based on reference signatures from the ImmGen database. Cytotoxic gene expression signatures in CD8$^+$ T cells were quantified using AUCell[54] scoring for key effector genes (Gzma, Gzmb, Gzmh, Gzmk, Prf1, FasL, Ifng, Tnf, Nkg7, Gnly). (*Gzma*, *Gzmb*, *Gzmh*, *Gzmk*, *Prf1*, *FasL*, *Ifng*, *Tnf*, *Nkg7*, *Gnly*.)

Chronic *in vitro* exhaustion model

To induce chronic exhaustion, 5×10^5 CD8$^+$ T cells were stimulated with α-CD3/28 beads (1:1 bead-to-cell ratio) and 10 ng/mL IL-2 in 48-well flat-bottom plates at 37 °C and 5% CO_2, with or without 50 ng/mL IL-4 (Peprotech; 214-14). Cells were harvested, counted, and restimulated every 2 days under the identical conditions. On day 6, flow cytometry was performed to assess exhaustion markers. For intracellular cytokine analysis, monensin was added during the final 4 hours of culture.

Spatial Transcriptomics

The spatial transcriptomics workflow was performed using the Visium CytAssist Spatial Gene Expression for FFPE according to the manufacturer's protocoll (Workflow and reagents are described in detail in the 10x Genomics document, Doc ID: CG000520 Rev C and are also listed in the key resources table). The tissue was sectioned as described in Visium CytAssist Spatial Gene Expression for FFPE – Tissue Preparation Guide (10x Genomics document, Doc ID: CG000520 Rev C). 10 μm sections were placed on a Superfrost™ ultra plus slide (ThermoScientific; 10149870) and H&E-staining was performed upon deparaffinization as outlined in the manual. Sections were imaged using a Leica DMi8 microscope and coverslips were removed before H&E destaining and decrosslinking as described in the manufacturer's protocol. For probe hybridization the Visium Mouse Transcriptome Probe Set v1.0 (10x Genomics; PN-1000365) has been used. Post-hybridization wash, probe ligation and post-ligation wash were conducted according to manufacturer's instructions (10x Genomics document, Doc ID: CG000495 Rev E) The Visium CytAssist device was used to transfer the probes to a Visium CytAssist Spatial Gene expression slide with a capture area of 6,5mm × 6,5mm. Probe extension, probe elution and probe-based library construction were performed according to the manufacturer's library preparation protocol. Concentration of final libraries was assessed using the Qubit 2.0 Flex (Invitrogen) and average size was determined on a TapeStation 4150 (Agilent). Premade libraries were sequenced at Novogene (Cambridge, UK) aiming for approx. 50.000 reads per spot on the capture area. Preprocessed raw data were analyzed by Visium SpaceRanger pipeline (v. 2.1.0 with mm10-2020-A as reference) and pipeline output was used for visualization and further analysis by the licensed software Partek Flow according to the documentation available in Partek Flow (https://help.partek.illumina.com/partek-flow/tutorials/10x-genomics-visium-spatial-data-analysis/spatial-data-analysis-steps). Noise was reduced by filtering out features with value <1 in 99% of the cells followed by normalization (1. CPM (counts per million; 2. Add 1 and 3. Log 2.0), PCA for dimension reduction, graph-based clustering using the Louvain clustering algorithm with Partek Flow's default settings) and UMAP for visualization of the clusters.

TCGA dataset analysis

Polyamine Metabolism Gene Profiling

GEPIA2 (http://gepia2.cancer-pku.cn)[55] was used to analyze expression levels of genes involved in polyamine metabolism across different tumor types and matched normal tissues.

Survival prognosis analysis

Kaplan–Meier survival analyses for SKCM patients were performed using TIMER2.0 (https://cistrome.shinyapps.io/timer/)[56] (employing CIBERSORT algorithm[57]) to assess the impact of *CSNK2B* and *LILRB4* expression combined with T_{reg} cell infiltration. Patients were stratified into high (top 30%) and low (bottom 30%) expression/infiltration groups. All other Kaplan–Meier analyses based on gene expression or gene signatures were conducted using GEPIA2 with the same thresholds.

Gene correlation analysis

TIMER2.0 was used to assess gene-expression correlations in SKCM biopsies. Spearman's correlation coefficient was applied to quantify the strength.

Docking analysis

Molecular docking of spermidine (SMILES: NCCCCNCCCN) to the CK2β subunit (PDB:1JWH, chain D) was performed using SwissDock (https://www.swissdock.ch)[58] applying the Attracting Cavities (AC) method.[59] Docking parameters: box center [33, -16, -58], box size [55, 70, 45], moderate exhaustivity, 2 random initial conditions. Binding site visualization was carried out using UCSF Chimera.[27]

Immunohistochemistry

B16.F10 tumors of comparable size were isolated on day 15 after inoculation, fixed in formalin and embedded in paraffin. Paraffin slices (3-4 μm thick) were deparaffinized in xylene and rehydrated using graded alcohols. After antigen retrieval using Dako EnVision™ Flex Target Retrieval Solution low pH (pH 6.0; Dako; Agilent Technologies, Inc.), the samples were incubated with an anti-mouse CD31 (Abcam; 2802125) or anti-mouse BLIMP-1(Thermo Fisher; 1907437) antibody. Positive staining was visualized using Dako EnVision™ Flex HRP Magenta Chromogen. The number of $CD31^+$ vessels was counted per mm^2 using an Olympus BX51 microscope (Olympus, Tokyo, Japan). Images were taken using a Gryphax Subra camera (Jenoptik, Jena, Germany). For confirmation of the results, quantification was performed using ImageJ software.

qPCR analysis

Total RNA was extracted using the RNeasy Micro Kit (Qiagen) and quantified with a Bioanalyzer 2100 (Agilent) using the RNA 6000 Pico Chip Kit. Complementary DNA (cDNA) was synthesized using the qScriber cDNA Synthesis Kit (highQu; RTK0104). qPCR was performed on a StepOnePlus Real-Time PCR System (Applied Biosystems) using Hot Start Taq EvaGreen Mix (Axon; 27488), 0.8 μM of each primer, and 8 μL diluted cDNA per 20 μL reaction. *Hprt* was used as a reference gene.

Generation of mixed-BM chimeras

Mixed bone marrow (BM) chimeras were generated as previously described.[70] Chimeras were generated by transferring 4×10^6 BM cells (1:1 ratio of $CD90.2^+$ (*Csnk2b*$^{Treg-/-}$) and $CD90.1^+$ (*Csnk2b*$^{fl/fl}$) cells) into lethally irradiated (9.5 Gy) $CD90.1^+$ C57BL/6J recipients. Chimeras were analyzed ≥8 weeks post-reconstitution.

Mouse model of adoptive-transfer colitis

The adoptive transfer model of colitis was performed as previously described.[71] Briefly, naive $CD4^+CD25^-$ T cells (5×10^5) from $Ly5.1^+$ C57BL/6J mice were transferred i.p. into 6-8-week-old $RAG1^{-/-}$ recipients alone or with equal numbers of $CD4^+CD25^+$ T cells from *Csnk2b*$^{Treg-/-}$ or *Csnk2b*$^{fl/fl}$ mice. Mice were monitored weekly for body weight. Animals that dropped below 85% of their initial weight were euthanized and excluded from further analysis. Mice were age- and sex-matched and co-housed whenever possible.

T helper cell polarization

Naive $CD62L^+CD44^-CD4^+$ T cells (2×10^5) were cultured on α-CD3/CD28-coated plates (4 μg/mL each) with 10 ng/ml IL-4 (Miltenyi Biotec; 130-097-761), 10 ng/ml IL-2 (Miltenyi Biotec; 130-120-331), and 10 μg/ml α-IFN-γ for 72 hours (37°C, 5% CO_2 atmosphere, 96-well flat-bottom plates), then re-seeded (4×10^5) with or without 1 μM DMAT. T_H2 polarization was confirmed by GATA3 expression (day 4, >90% positive). IL-4 production was assessed on day 5 following 4-hour stimulation with PMA (20 ng/mL), ionomycin (1 μM), and monensin by flow cytometry. For T_H1 differentiation, naive $CD62L^+CD44^-CD4^+$ T cells (2×10^5) were cultured on α-CD3/CD28-coated plates (α-CD3: 4 μg/mL; α-CD28: 8 μg/mL) with 10 ng/mL IL-12 (Miltenyi Biotec; 130-096-707), 10 ng/mL IL-2, and 10 μg/mL α-IL-4 (Miltenyi Biotec; #130-095-709) for 72 hours (37°C, 5% CO_2 atmosphere, 96-well flat-bottom plates).

$CD8^+$ T cell culture

$CD8^+$ T cells (5×10^5) were stimulated with α-CD3/CD28 beads (1:1 bead-to cell ratio) and IL-2 (10 ng/mL) with or without 1 μM DMAT (37°C, 5% CO_2 atmosphere, 48-well flat-bottom plates). Production of IFN-γ, TNF-α, and Granzyme B was assessed at 24, 48, and 72 hours by flow cytometry following 4-hour stimulation with PMA (20 ng/mL), ionomycin (1 μM), and monensin.

Suppression assays

T_H1 or $CD8^+$ T cells (2×10^5) were co-cultured with $CD11c^+$ splenic cells (4×10^5) and soluble α-CD3 (4 μg/mL) in the presence of $CD4^+CD25^+$ T cells at effector-to-Treg cell ratios of 1:2-1:8. IFN-γ production was measured by ELISA after 72 hours of co-culture. For proliferation assays, $CD8^+$ T cells were pre-labeled with CellTrace Violet (ThermoFisher; C34571) according to the manufacturer's instructions and proliferation assessed by flow cytometry under identical conditions.

QUANTIFICATION AND STATISTICAL ANALYSIS

Statistical analyses were performed using GraphPad Prism (version 10.3.0), unless otherwise specified. Data are presented as mean ± standard deviation (SD), unless noted differently in the figure legends. Group comparisons were conducted using unpaired

Student's t-test with Welch's correction to account for unequal variances. A 95% confidence interval was applied throughout, and adjusted p-values < 0.05 were considered statistically significant. The specific statistical tests and sample sizes for each experiment are provided in the respective figure legends. Survival analyses were conducted using the Kaplan–Meier method, with group comparisons performed using the log-rank (Mantel–Cox) test and Cox proportional hazards regression. Correlations were assessed using Spearman's rank correlation coefficient. For *in vivo* experiments, researchers were blinded to group allocation, except for treatment studies where treatment administration and tumor size measurements were performed at different time points by separate individuals to allow for partial blinding. Sample sizes were determined based on preliminary experiments to ensure adequate statistical power. Flow cytometry datasets with fewer than 50 events in the final gated populations were excluded from analysis.